



Contents lists available at ScienceDirect

Nuclear Instruments and Methods in Physics Research A

journal homepage: www.elsevier.com/locate/nima

Review

Electromagnetic calorimetry

R.M. Brown, D.J.A. Cockerill*

Rutherford Appleton Laboratory, STFC, Chilton, Didcot, Oxon, OX11 0QX, UK

ARTICLE INFO

Available online 1 April 2011

Keywords:
 Calorimetry
 Electromagnetic
 Principles
 Resolution
 Particle
 Nuclear
 Neutrino
 Collider

ABSTRACT

Electromagnetic calorimetry forms a key element of almost all current high energy particle physics detectors and has widespread application in related experimental fields such as nuclear physics and astro-particle physics. It will play a particularly important role in the latest generation of experiments at the CERN Large Hadron Collider (LHC), where it is expected that high energy electrons and photons will provide some of the clearest signatures for new discoveries. This article introduces the basic concepts underlying electromagnetic calorimetry and illustrates how these principles have been applied in recent and current detector designs, explaining the connection between technical choices and specific physics goals. Designs are described in sufficient detail to demonstrate the compromises that have to be made in achieving optimum performance within practical constraints. The main emphasis is on the LHC experiments, which provide outstanding examples of the state-of-the-art. Selected examples from other domains, such as nuclear physics and neutrino experiments are also considered and particular attention is given to calorimeter design studies for the proposed International Linear Collider (ILC) where the concept of Particle Flow Analysis is being used as a guiding influence in the overall detector optimization.

© 2011 Published by Elsevier B.V.

Contents

1. General introduction	48
2. General principles	48
2.1. Energy loss by electrons and photons	48
2.2. Electromagnetic cascades	49
2.3. Shower containment	49
3. Energy resolution	50
3.1. Introduction	50
3.2. Energy resolution of homogeneous calorimeters	50
3.3. Energy resolution of sampling calorimeters	51
4. Calorimetry for particle physics	51
4.1. Introduction	51
4.2. Homogeneous calorimeters	51
4.2.1. The CMS crystal calorimeter	51
4.2.2. The ALICE PHOS	55
4.2.3. The NA48 liquid krypton calorimeter	55
4.2.4. The MEG liquid xenon calorimeter	57
4.3. Sampling calorimeters	59
4.3.1. The ATLAS liquid argon ACCORDION sampling calorimeter	59
4.3.2. The LHCb electromagnetic calorimeter	61
4.3.3. The ALICE EMCAL	64
4.3.4. The KLOE sampling calorimeter	66
4.4. Particle flow calorimetry at the International Linear Collider	68
4.4.1. Introduction	68
4.4.2. The ILD electromagnetic calorimeter	69
4.4.3. CALICE studies of a prototype fine-grained ECAL	69

* Corresponding author.

E-mail address: d.cockerill@cern.ch (D.J.A. Cockerill).

5.	Calorimetry for nuclear physics	71
5.1.	Introduction	71
5.2.	The application of γ -ray spectroscopy to the study of exotic nuclei	71
5.2.1.	The AGATA tracking calorimeter	72
5.3.	Future applications of germanium detector technology	76
6.	Calorimetry for low energy neutrino physics	76
6.1.	Liquid scintillator calorimeters	76
6.1.1.	The Borexino liquid scintillator detector	77
6.1.2.	The KamLAND liquid scintillator detector	77
6.1.3.	Liquid scintillator summary	78
7.	Summary	79
	Acknowledgements	79
	References	79

1. General introduction

In particle physics, the term “calorimeter” is used to describe a device that absorbs a substantial fraction of the energy of an incident particle and produces a signal with amplitude proportional to that energy. Absorption of the incident energy is via a cascade process, whereby a total number, n , of secondary particles is produced. The average value of n is proportional to the incident energy, E_0 :

$$\langle n \rangle \propto E_0 \quad (1)$$

An important factor governing the energy resolution arises from fluctuations on the detected signal and therefore grows as \sqrt{n} . Thus, in the limiting case that this contribution dominates, the energy dependence of the energy resolution scales as:

$$\frac{\sigma_{E_0}}{E_0} \propto \frac{1}{\sqrt{n}} \propto \frac{1}{\sqrt{E_0}} \quad (2)$$

The depth required to contain the cascade of secondary particles grows only logarithmically with energy. This may be contrasted with the case of a magnetic spectrometer, whose length (for a given magnetic field integral) would need to increase linearly with momentum in order to keep the relative momentum resolution constant.

The combination of logarithmic scaling in size and improving relative energy resolution with increasing energy enables calorimeters to make a uniquely powerful contribution to experiments at the energy frontier. Furthermore, in the case of neutral particles, a calorimeter provides the most practical method of detection and energy measurement. As a consequence, electromagnetic calorimetry forms a key element of almost all current high energy particle physics detectors and it will play a particularly important role in the latest generation of experiments at the CERN Large Hadron Collider (LHC), where it is expected that high energy electrons and photons will provide some of the clearest signatures for new discoveries. The technique also finds widespread application in related experimental fields such as nuclear physics and astro-particle physics.

This article focuses on the practicalities of turning detector concepts into working calorimeters, explaining the connection between technical choices and specific physics goals. Designs are described in sufficient detail to demonstrate the compromises that have to be made in achieving optimum performance within practical constraints. Illustrative examples are selected from recent, current, and projected experiments. The main emphasis is on the LHC experiments, which provide outstanding examples of the state-of-the-art. Selected examples from other domains, such as nuclear physics and neutrino experiments are also considered and particular attention is given to calorimeter design studies for the proposed International Linear Collider (ILC) where

the concept of Particle Flow Analysis is being used as a guiding influence in the overall detector optimization.

Section 2 of this article introduces the general physical principles that govern the development and propagation of electromagnetic showers in dense media. Section 3 describes the distinguishing features of “homogeneous” and “sampling” calorimeters and discusses the properties that limit energy resolution for these two general classes of calorimeter. Section 4 lists illustrative examples of calorimeters that have been built, or are planned, for accelerator-based particle physics experiments. Section 4.2 focuses on examples of homogeneous calorimeters, Section 4.3 presents sampling designs, and Section 4.4 discusses recent developments in particle flow analysis, directed towards experiments at a future electron–positron linear collider. Applications of calorimetry in nuclear physics are described in Section 5, Section 6 discusses the use of liquid scintillator in calorimetric measurements of neutrino interactions, and Section 7 gives a summary.

2. General principles

2.1. Energy loss by electrons and photons

At high energies, electrons¹ traversing matter lose energy primarily through the radiation of photons (“bremsstrahlung”), the mean rate of energy loss increasing almost linearly with energy. Bremsstrahlung occurs principally in the electric field of atomic nuclei and the amplitude for the process is approximately proportional to the nuclear charge, Z . Thus the energy loss per unit depth is:

$$-\frac{dE}{dx} \cong \frac{E}{X_0} \quad (3)$$

where X_0 is the radiation length, which determines the scale characterizing the rate of loss in a given material and has a value given by the following approximate expression [1]:

$$X_0 = \frac{A}{4\alpha N_A Z^2 r_e^2 \ln(183Z^{1/3})} \quad (4)$$

where A is the atomic mass, r_e the classical electron radius and N_A is Avogadro’s number.

However, bremsstrahlung also occurs through interaction of the incident electrons with electrons in the material. Since there are Z electrons per nucleus, the cross-section receives an additional term proportional to Z . The atomic electrons have the additional effect of partially screening the nuclear charge. An approximate expression that accounts for these effects and gives a

¹ In this article, the term “electron” sometimes refers to both “electron” and “positron”. The usage should be clear from the context.

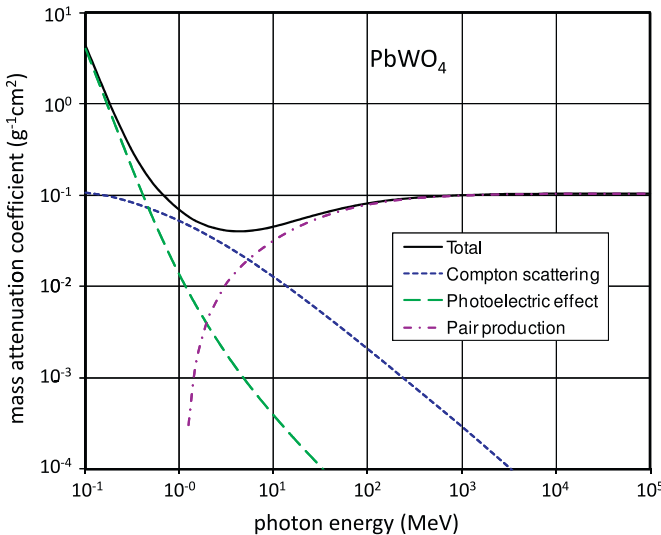


Fig. 1. Energy dependence of the photon mass attenuation coefficient in lead tungstate (data from NIST XCOM data base [3]).

good description of the data is the following [2]:

$$X_0 = \frac{716.4A}{Z(Z+1)\ln(287/\sqrt{Z})} \text{ gcm}^{-2} \quad (5)$$

For sufficiently energetic photons, the primary mechanism for interaction with matter is pair production in the nuclear Coulomb field. At high energies, the process can occur at relatively large distances from a nucleus, and electron screening of the nuclear charge influences the cross-section. The bremsstrahlung and pair production processes are closely related and, in the high energy limit, the mean free path for pair production by photons may be expressed in terms of the radiation length:

$$L_{\text{pair}} = \frac{9}{7} X_0 \quad (6)$$

This expression is valid down to ~ 1 GeV for high Z materials.

Energy loss by electrons through ionization makes an important contribution to the total energy loss at low energies. Above the ionization minimum, the rate of loss rises logarithmically with energy. In contrast, as seen in Eq. (3), the rate of loss through bremsstrahlung rises almost linearly with energy.

The critical energy, E_c , may be defined as the energy for which, in a given material, the rates of energy loss through ionization and bremsstrahlung are equal. For all but the lightest elements ($Z \leq 12$), the critical energy is given to an adequate approximation by the expression:

$$E_c = \frac{550}{Z} \text{ MeV} \quad (7)$$

and thus has values in the range from a few to a few tens of MeV.

Finally it may be noted that in heavy materials, for photons below a few MeV, Compton scattering and the photoelectric effect make the dominant contributions to energy loss, as shown for lead tungstate in Fig. 1. Of particular note is the minimum in the mass attenuation coefficient that occurs at a photon energy of ~ 4 MeV, corresponding to a mean free path of $\sim 3.4X_0$.

2.2. Electromagnetic cascades

A high energy electron or photon incident on an absorber medium of sufficient depth will generate an electromagnetic cascade through the processes of bremsstrahlung and pair

production, the initial rate of growth with depth in the number of secondary particles depending on the radiation length of the material. As the cascade develops, the average energy carried by an individual charged particle decreases. When this energy falls to the critical energy, the electrons are brought to rest by energy loss through ionization and excitation. The depth at which the shower maximum occurs depends on the incident energy and the nature of the incident particle (electron or photon), and is given approximately by the expression:

$$t_{\max} = \ln\left(\frac{E_0}{E_c}\right) + c_i \quad (8)$$

where t_{\max} is the depth of the shower maximum in units of X_0 and c_i has the value -0.5 for electrons and $+0.5$ for photons.

Eq. (8) illustrates the logarithmic increase with energy in the depth of shower development, mentioned in Section 1.

The profile of energy loss versus depth can be approximated by the empirical expression:

$$\frac{dE}{dt} = C t^\alpha e^{-\beta t} \quad (9)$$

where t is the depth in the material in units of X_0 , and C , α and β are parameters to be determined empirically.

The form of the expression can be understood in terms of an initial power law growth in number of cascade particles (and hence the rate of energy loss), up to the shower maximum, followed by an exponential fall off as they are absorbed.

An improved parameterization of the shower profile has been obtained by comparison with simulations of the electromagnetic cascades obtained with the EGS Monte Carlo programme:

$$\frac{dE}{dt} = \frac{E_0 \beta (\beta t)^{\alpha-1} e^{-\beta t}}{\Gamma(\alpha)} \quad (10)$$

where $\Gamma(\alpha)$ is the Euler Γ function.

2.3. Shower containment

Important properties influencing the design of a practical calorimeter are the longitudinal and lateral extent of showers in the chosen absorber medium, over the relevant range of incident energies. The depth of absorber required is dictated by the need to keep longitudinal leakage of showers below a certain limit, since fluctuations on the leakage will degrade the energy resolution. Several parameterizations have been proposed to enable the containment depth to be estimated, for example [2]:

$$\langle L_{98} \rangle = 2.5 t_{\max} \quad (11)$$

where $\langle L_{98} \rangle$ is the absorber thickness in units of X_0 , required to contain, on average, 98% of the shower energy.

The tail of the cascade is associated with photons with energies of a few MeV, in the region corresponding to the minimum of the mass attenuation coefficient. This motivates an alternative parameterization of the form:

$$\langle L_{98} \rangle = t_{\max} + 4\lambda_{\text{att}} \quad (12)$$

where λ_{att} is associated with the exponential decrease following the shower maximum.

The value of λ_{att} depends on the material. Experimentally, it is found to be similar to the maximum value of the photon mean free path, taking values in the range $\lambda_{\text{att}} \cong (3.4 \pm 0.5)X_0$ [4].

The rms spread in the shower energy leaking from the back of an absorber is roughly half the mean value of the leakage. Thus for an electromagnetic calorimeter aiming to achieve a resolution of better than 1% at high energy, even an absorber thickness as large as $\langle L_{98} \rangle$ will not be sufficient.

The transverse spread of an electromagnetic cascade arises mainly from the multiple scattering of electrons and is

characterized by the Molière radius [5,6], which is given to a good approximation by

$$R_M = \frac{21}{E_c(\text{MeV})} X_0 \text{ g cm}^{-2} \quad (13)$$

On average, 95% of the shower energy is contained within a cylinder of radius $2R_M$.

The lateral spread of showers is an important consideration in deciding the optimum transverse dimensions of individual calorimeter cells. There is no advantage in making the cell dimensions much smaller than R_M . On the other hand, ensuring that showers spread across several cells leads to an improved estimate of the transverse position of impact of the incident particle.

3. Energy resolution

3.1. Introduction

Calorimeters designed for high energy physics experiments may be broadly classified into one of two types: sampling calorimeters and homogeneous calorimeters. Sampling calorimeters consist of layers of a dense passive absorber (such as lead or copper), interleaved with active detector layers (such as silicon, plastic scintillator or liquid argon). A notable example of this type of construction is the electromagnetic calorimeter of the ATLAS experiment at the LHC, consisting of lead converter foils immersed in liquid argon. In a homogeneous calorimeter, a single medium (such as liquefied xenon or a crystal scintillator) serves as both the absorbing medium and the detector. The largest crystal electromagnetic calorimeter ever constructed is the “ECAL” of the CMS experiment at the LHC, which employs lead tungstate crystals. The ATLAS and CMS calorimeters are discussed in more detail below.

The energy dependence of the energy resolution may be parameterized as the quadratic sum of three terms:

$$\frac{\sigma_E}{E_0} = \frac{a}{\sqrt{E_0}} \oplus \frac{b}{E_0} \oplus c \quad (14)$$

The first term, with coefficient a , is the “stochastic term”, arising from fluctuations in the number of signal generating processes (together with possible additional effects such as fluctuations in the measurement of that signal).

The second term, with coefficient b , is usually referred to as the noise term. It receives contributions not only from noise in the readout electronics, but also from effects such as “pile-up” (simultaneous energy deposition by uncorrelated particles).

The third term is the “constant term” with coefficient c . It arises from several effects including:

- imperfections in calorimeter construction (dimensional tolerances, etc.);
- non-uniformities in signal collection;
- channel-to-channel calibration errors;
- fluctuations in longitudinal energy containment; and
- fluctuations in energy lost in inert material, before or within the detection volume.²

A primary goal of calorimeter design is to find, for a given application, the optimal compromise between the contributions from the three terms. In the case of high resolution electromagnetic calorimeters, the energy resolution at high energy is usually dominated by the constant term.

In the following two sections, factors imposing intrinsic limits on achievable energy resolutions are presented. Additional effects which cause the performance of real designs to fall short of the ideal limits will be illustrated with some representative examples in later sections.

3.2. Energy resolution of homogeneous calorimeters

In homogeneous calorimeters, the absorber also acts as the detection medium. Consequently, the amplitude of the produced signal is proportional to the total track length, T_{tot} , of charged particles with energies above threshold for detection. Effectively, the incident electron or photon behaves as would a single ionizing particle of the same energy, losing all its energy through ionization by an amount equal to the critical energy for every radiation length traversed. Thus:

$$T_{tot} = \sum_{i=1}^N T_i = \left(\frac{E_0}{E_c} \right) X_0 \quad (15)$$

The produced signal will be the sum of a large number of discrete “signal quanta” whose nature depends on the detection medium. For example, in a crystal calorimeter, the signal quantum will be a scintillation photon. If the average length of track, traversed by a charged particle between the production of each signal quantum, is defined as L_{sig} , then the mean total number of signal quanta produced is

$$\langle n \rangle = \frac{T_{tot}}{L_{sig}} \quad (16)$$

The “intrinsic energy resolution” is then determined by fluctuations of n about the mean value. At first sight, one might expect the variance on n to be governed by Poisson statistics, thus for large n :

$$\frac{\sigma_E}{E_0} = \frac{\sqrt{n}}{n} = \sqrt{\frac{L_{sig}}{T_{tot}}} \quad (17)$$

However, T_{tot} is constrained by the incident energy, thus fluctuations on n may be reduced. This is taken into account by introducing the “Fano factor”, F :

$$\frac{\sigma_E}{E_0} = \frac{\sqrt{Fn}}{n} = \sqrt{\frac{FL_{sig}}{T_{tot}}} \quad (18)$$

In the case of a semiconductor detector (for example a high-purity germanium detector of the type used in γ -spectroscopy), where the signal quantum is an electron-hole pair, almost all of the energy deposited in the absorber contributes to the creation of signal quanta. Thus n is strongly constrained, F has a relatively small value (~ 0.1) [7], and a very good energy resolution results.

In contrast, in a crystal calorimeter, only a very small fraction of the deposited energy leads to the production of scintillation photons, thus n is essentially unconstrained. Furthermore, the photons are not detected directly, but must be transported to a photodetector (suffering losses through absorption and optical matching) and converted, with further loss, to photoelectrons. Thus in this case:

$$\frac{\sigma_E}{E_0} = \sqrt{\frac{Fn_{pe}}{n_{pe}}} \quad (19)$$

where n_{pe} is the number of detected photoelectrons and $F \sim 1$. An additional contribution to the Fano factor may arise if a photodetector with internal gain is used in order to give a more favourable signal-to-noise ratio in the associated readout electronics. For example, in the case of an avalanche photodiode, internal

² If the amount of material is substantial, this effect may also degrade the stochastic term.

gain fluctuations may increase the effective value of F to ~ 2.4 for the crystal/photodetector combination.

3.3. Energy resolution of sampling calorimeters

In sampling calorimeters, most of the energy is deposited in the passive absorber layers. The energy deposited in each absorber layer is estimated by measuring a signal produced in the adjacent downstream active layer, which is proportional to the number of charged particles crossing that layer. An important contribution to the stochastic term in the energy resolution function is therefore caused by sampling fluctuations, arising from variations in the total number of charged particles, n_{ch} , crossing the active layers. This number increases with the incident energy and with the fineness of the sampling. Thus:

$$n_{ch} \propto \frac{E_0}{t_{abs}} \quad (20)$$

where t_{abs} is the thickness of each absorber layer.

If each sampling is statistically independent of the rest (i.e. if the absorber layers are sufficiently thick that the effect of single particles traversing more than one detector layer can be neglected), then the sampling contribution to the stochastic term is

$$\frac{\sigma_E}{E_0} \propto \frac{1}{\sqrt{n_{ch}}} \propto \sqrt{\frac{t_{abs}}{E_0}} \quad (21)$$

Thus the energy resolution improves as t_{abs} is decreased. However, an impractically large number of samplings (of order 100) would be required for the energy resolution to approach that of a homogeneous device. Typically, the sampling fluctuations contribute $\sim 10\%/\sqrt{E_0}$ (E_0 in GeV) to the stochastic term.

4. Calorimetry for particle physics

4.1. Introduction

The intrinsic limits on energy resolution discussed above cannot be fully reached in practice because of additional effects that inevitably arise in the realization of practical and affordable designs, integrated with other sub-systems into an experiment. Thus compromises must be made and optimization of the performance will be strongly influenced by the emphasis placed

on specific physics goals. The main emphasis in this section is on calorimeters that have been constructed for the experiments at the LHC, since, for several leading technologies, they represent the state-of-the-art for applications in accelerator-based particle physics experiments and serve as outstanding examples of what can actually be achieved. In addition, three examples are given from experiments at other accelerators, to illustrate techniques that have been used to achieve very good energy resolution, particularly at lower energies.

4.2. Homogeneous calorimeters

Two experiments at the LHC (CMS and ALICE) incorporate homogeneous electromagnetic calorimeters, motivated by the desire to achieve very good energy resolution. In both cases, the choice has been to use lead tungstate scintillating crystals coupled to large area APDs. Details are given in the following two sub-sections. CMS is discussed at some length, since it provides an excellent demonstration of the link between intrinsic effects and the performance achieved in a real device.

4.2.1. The CMS crystal calorimeter

4.2.1.1. General description. Compact Muon Solenoid (CMS) [8,9] is a general purpose detector, designed to be sensitive to a wide range of possible new physics. It incorporates a high resolution electromagnetic calorimeter (ECAL) comprising $\sim 76\,000$ lead tungstate (PbWO_4) crystals covering almost 4π of solid angle [9]. The benchmark that has been used to optimize the design of the ECAL is the potential to discover a Higgs boson in the mass region below 130 GeV, by measuring the decay $H \rightarrow \gamma\gamma$. Since the intrinsic decay width is expected to be small, the measured width, which has a crucial influence on the significance of the signal above the expected large background, comes entirely from the ECAL energy resolution. The design goal is an energy resolution of better than 0.5% for photons above 100 GeV. In addition to having high resolution, the ECAL must be reliable, fast, have high granularity and be radiation-resistant.

The ECAL comprises a Barrel section and two Endcaps (Figs. 2 and 4). The Barrel is divided into two halves, each divided into 18 φ -sectors ('Supermodules') containing 1700 crystals. Each Endcap is divided vertically into two 'Dees', each with 3662 crystals grouped in 5×5 sub-units ('Supercrystals'). All crystals are tapered and are arranged in a projective geometry, pointing approximately 3° away from the mean beam collision point, to minimize the effect of

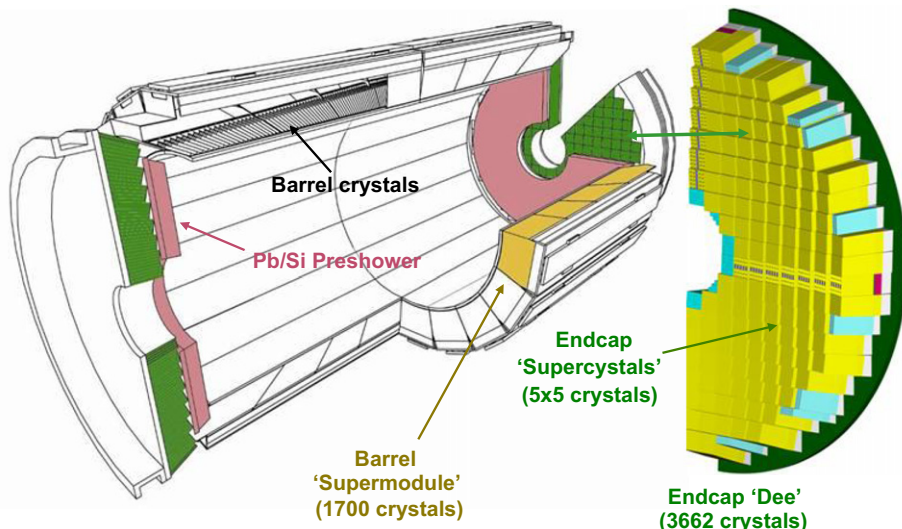


Fig. 2. Schematic layout of the CMS electromagnetic calorimeter.

inter-crystal gaps. A Preshower detector, consisting of two orthogonal planes of silicon strip sensors interleaved with lead ($3X_0$ in total); improves γ/π^0 discrimination in the Endcap regions. The crystals in the Barrel are typically $25 \times 25 \text{ mm}^2$ in cross-section and 230 mm ($25.8X_0$) long; in the Endcap they are $30 \times 30 \text{ mm}^2$ in cross-section and 220 mm ($24.7X_0$) long. The Endcap crystals are shorter since they are preceded by the Preshower detector. In order to minimize the amount of inert material in front of the calorimeter, it is located within the magnetic field volume of the CMS 3.8 T superconducting solenoid.

Lead tungstate [10] has a short radiation length (0.89 cm), and a small Moilère radius (2.19 cm). This permits a design that has high granularity combined with compactness, a very important consideration for a detector located within the magnetic field volume. Scintillation emission is fast (80% of light within 25 ns) and peaks in the blue (425 nm), simplifying photo-detection. However, the light yield is rather low ($\sim 70 \text{ photons/MeV}$), and varies with temperature ($-2\text{}/^\circ\text{C}$ at $18\text{ }^\circ\text{C}$). Thus the photo-detectors must have internal gain (in a strong magnetic field) and the temperature of the calorimeter must be stabilized to better than $0.1\text{ }^\circ\text{C}$.

In the Barrel section, the photo-detectors are Avalanche Photodiodes (APDs) [11]. They are each $5 \times 5 \text{ mm}^2$ in area and are mounted in pairs, thus covering approximately 8% of the rear

face of each crystal. They have a quantum efficiency of 75% at the emission wavelength and are operated at a gain of 50. Vacuum Photo-Triodes (VPTs) are deployed in the Endcaps, where radiation levels are higher and the magnetic field direction, which is within 18° of the crystal axes, is favourable for their use [12]. VPTs are photomultipliers with a single gain stage, and these particular devices have a radiation resistant UV glass window and are 280 mm^2 in effective area. Thus they cover approximately 30% of each crystal end-face. They have a typical quantum efficiency of 20% and gain of 10 at 3.8 T. The photo-detector signals are processed with radiation-resistant on-detector electronics [13] implemented in IBM 0.25 μm technology. The preamplifiers/amplifiers have a shaping time of 40 ns. The electronic noise is equivalent to 40 MeV/channel in the Barrel and 150 MeV/channel in the Endcaps. The noise summed over a cluster of channels scales as \sqrt{n} , where n is the number of crystals in the cluster.

Lead tungstate is radiation-resistant up to very high integrated doses, nevertheless colour centres form and self-anneal under irradiation at room temperature, causing the light output to vary with dose rate. Changes in crystal transparency are therefore tracked with a laser monitoring system, normalized by a system of very stable silicon photodiodes diodes. Changes in optical transmission measured with a blue laser (440 nm) are strongly correlated with changes in the yield of scintillation light under irradiation, allowing precise corrections to be made (Fig. 3).

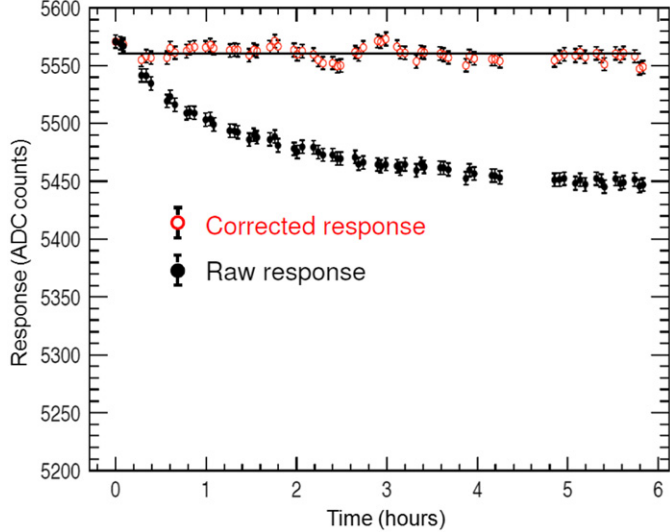


Fig. 3. Response to high energy electrons as a function of time, before and after correction with the laser monitoring system.

4.2.1.2. Expected energy resolution. Stochastic term: In Section 3.2 it was noted that, for an ideal crystal calorimeter, the stochastic term in the resolution function (Eq. (14)) is dominated by statistical fluctuations in the number of detected photoelectrons, with $F=1$. In the Barrel region of the CMS ECAL, an energy deposit of 1 GeV in a lead tungstate crystal produces, on average ~ 4500 photoelectrons in the pair of APDs mounted on the rear face. When operated at the normal gain of 50, fluctuations in the APD amplification process ("excess noise") result in an overall value for F of 2.4. Thus the "intrinsic" contribution to the stochastic term, arising from photoelectron statistics is expected to be:

$$a_{pe} = \sqrt{\frac{F}{n_{pe}}} = \sqrt{\frac{2.4}{4500}} = 2.3\% \quad (22)$$

However, this assumes complete lateral containment of the showers. In practice, the energy summation is restricted to crystals clustered close to the core of a shower, to reduce the effects of electronic noise and pile-up. As a result, fluctuations in the energy leaking into surrounding crystals make an additional contribution to the stochastic term. In the case of a summation over 9 crystals in a 3×3 array, this extra contribution is expected to correspond to

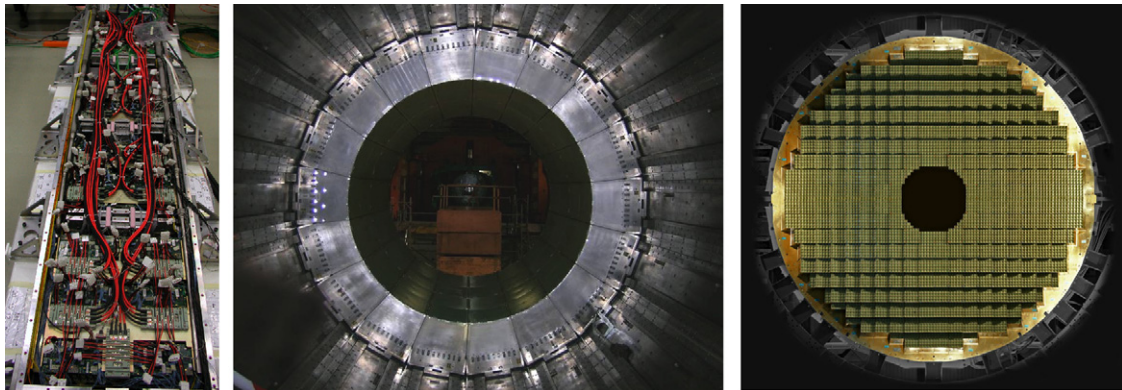


Fig. 4. Photographs of the CMS crystal ECAL showing, from left to right: a rear view of a Barrel supermodule during assembly; a complete half-barrel of 18 supermodules installed in CMS; a montage, showing front views of two Endcap Dees with the front covers removed, revealing the supercrystals and individual crystals.

$a_{leak} \approx 2.0\%$, resulting in an overall stochastic term:

$$a = a_{pe} \oplus a_{leak} = 3.0\% \quad (23)$$

Noise term: The amplitude from a single channel of the ECAL is calculated from up to 10 pulse height samples made at 25 ns intervals, including measurements made immediately preceding the signal pulse. This allows the baseline correction (or “pedestal subtraction”) to be made event-by-event and channel-by-channel. Using this method of signal reconstruction, it has been observed that there is no correlation of the electronic noise in adjacent channels. As a result, the total noise summed over the cluster of crystals is just a factor $\sqrt{n_{cl}}$ greater than the noise in a single channel, where n_{cl} is the number of channels in the cluster. Thus for clusters consisting of 3×3 arrays of crystals, the electronic noise in the Barrel is expected to result in an initial value of the noise term: $b = 120$ MeV.

During the course of the experiment, neutron irradiation will cause the leakage currents in the APDs to rise, increasing the electronic noise. The additional contribution is expected to be equivalent to 8 MeV/channel after one year of operation at $10^{33} \text{ cm}^2 \text{ s}^{-1}$ and 30 MeV/channel after a further year at $10^{34} \text{ cm}^2 \text{ s}^{-1}$ [13].

During LHC operation at high luminosity, b will receive an important contribution from event pile-up. The magnitude of this will depend on the LHC luminosity and the chosen cluster size. It will vary across the solid angle covered by the ECAL, being largest in the forward regions. At a luminosity of $10^{34} \text{ cm}^2 \text{ s}^{-1}$, the pile-up noise in the central part of the Barrel ($\eta=0$)³ is expected to be ~ 95 MeV and in the mid-region of the Endcaps ($\eta=2$) it is expected to be 525 MeV for (5×5) clusters of crystals.

Constant term: Various potential contributions to the constant term were listed in Section 3.1, for example the effect of errors in the channel-to-channel inter-calibration. Before installation, nine of the 36 supermodules of the ECAL Barrel section were exposed to high energy electrons (90 and 120 GeV), in a geometrical configuration that reproduced the incidence of particles during CMS operation [14]. A repeat exposure of one of the Supermodules indicated that the results are reproducible to within 0.2%. In addition, all 36 Supermodules were operated in turn on a cosmic ray stand for a period of about one week. A muon traversing the full length of a crystal deposits energy of approximately 250 MeV yielding further inter-calibration information. A comparison of the cosmic ray and high energy electron data demonstrates that the average precision of the cosmic ray inter-calibration is 1.5%. For both the Barrel and the Endcap sections, the final inter-calibration precision will be achieved *in situ* with high energy electrons and photons from physics events. Ultimately, the contribution to the constant term from the inter-calibration error is expected to be of order 0.4%.

A potentially important contribution to the constant term can arise from variations in light collection efficiency as a function of depth in a crystal. Such effects could be caused by optical absorption or be a consequence of the geometrical shape of the crystals. In the presence of such longitudinal non-uniformities, fluctuations in the depth of the shower maximum broaden the measured width of the energy distribution. Monte Carlo modelling of the Barrel crystals has shown that variations in light collection must be kept below $0.5\% X_0$ in the region of the shower maximum ($\sim 8 X_0$ from the front of the crystal) in order to keep the associated contribution to the constant term less than 0.3%. It has been found empirically that the required light-collection uniformity is achieved by polishing three of the longitudinal faces of the crystals and roughening the fourth face by a specified amount,

³ η is the pseudorapidity, defined by the relation: $\tanh \eta = \cos \theta$, where θ is the polar angle wrt the beam axis.

Table 1

Contributions to the energy resolution function expected at high luminosity ($10^{34} \text{ cm}^2 \text{ s}^{-1}$), in the Barrel section of the ECAL ($\eta=0$), summing over (3×3) clusters of crystals.

Stochastic term (a)	Lateral containment	2.0%
	Photoelectron statistics	2.3%
	Total stochastic term	3.0%
Noise term (b)	Electronics noise	120 MeV
	APD Leakage noise	90 MeV
	Pile-up noise	60 MeV
	Total noise term	160 MeV
Constant term (c)	Longitudinal non-uniformity	0.3%
	Inter-calibration errors	0.4%
	Total constant term	0.5%

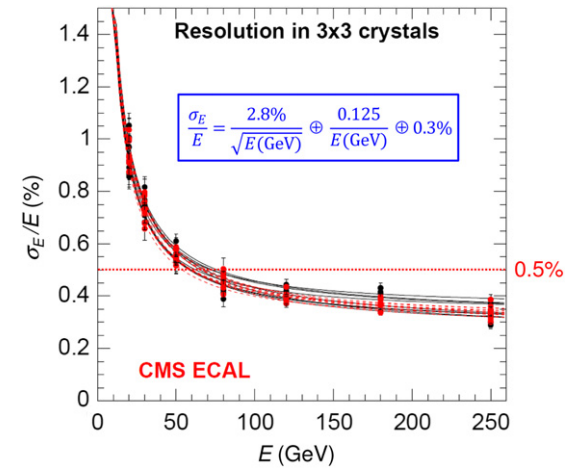


Fig. 5. The relative energy resolution versus energy obtained with a fully equipped Barrel supermodule exposed to a beam of high energy electrons. The energy is summed over 3×3 arrays of crystals, with the electron impact point required to lie within a $4 \times 4 \text{ mm}^2$ area, centred on the central crystal. Each curve corresponds to a different central crystal. A fit of the form given by Eq. (14), to the average of the curves, is given in the inserted panel. The horizontal dotted line indicates the CMS design goal of an energy resolution of better than 0.5% for high energy photons.

and by covering the inner surfaces of the sleeves supporting the crystals with a highly reflective coating.

The lengths of the crystals used in CMS ($25 X_0$ in the case of the Barrel crystals) is sufficient to ensure that fluctuations in shower leakage from the rear surface makes a negligible contribution to the constant term.

The various contributions to the energy resolution function are summarized in Table 1.

4.2.1.3. Measured energy resolution. Prior to installation in CMS, a fully equipped Barrel supermodule was studied using a beam of high energy electrons [15]. Measurements of the energy resolution were made at 7 energies in the range from 20 to 250 GeV. Fig. 5 shows a typical set of results obtained for (3×3) clusters centred on a number of different crystals, with the electron impact point required to be within a $4 \times 4 \text{ mm}^2$ region at the centre of the central crystal. The dashed curve overlying the solid curves has parameter values: $a = 2.8\%$, $b = 125$ MeV and $c = 0.3\%$ for the stochastic, noise and constant terms, respectively. These coefficients give a good representation of the average trend observed for this set of crystals and are in agreement with the expected values shown in Table 1, taking into account the absence of pile-up and APD leakage contributions to the noise, and the very good inter-calibration precision possible in the test beam.

The results shown in Fig. 5 are important in demonstrating that the energy resolution reaches the performance limits set by

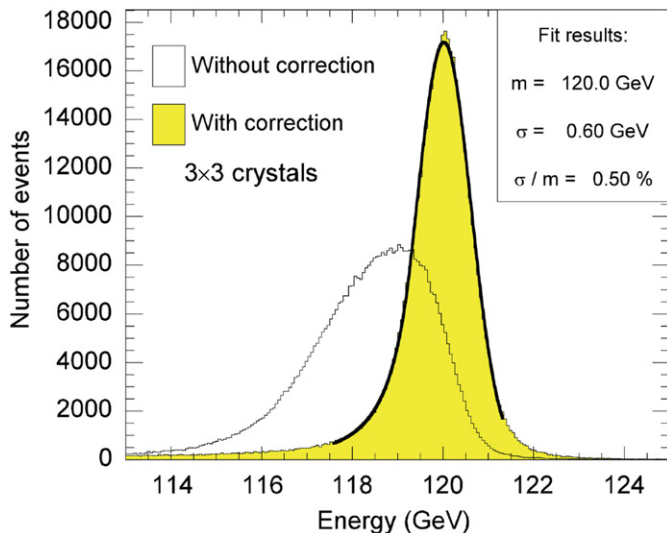


Fig. 6. The reconstructed energy distribution for 120 GeV electrons, averaged over impact points spanning several crystals. The open histogram is before a position-dependent correction has been applied, the filled histogram is after correction.

the constraints of the design, but they do not apply directly to the situation that will be encountered in CMS, where particles will strike the surface of the ECAL at randomly distributed points. To reproduce this situation, the electron energy was set to 120 GeV and runs were recorded with the beam centred successively on a set of impact points distributed over a region spanning several crystals in both x and y . The results were then combined to emulate the situation of a uniform impact distribution. The resultant distribution of the reconstructed energy is shown as the open histogram in Fig. 6 and has a width ~ 2.5 times greater than that obtained for central impacts.

The degradation in resolution is caused by variations in the mean energy loss through lateral leakage. The selection of crystals to be included in the energy summation is made by identifying the crystal with the largest energy and choosing the 3×3 cluster that has this crystal at the centre. The fraction of the total energy contained within the 3×3 array varies with the position of impact of the incident particle within the central crystal. As the point of impact is moved away from the centre of the central crystal, less energy is lost from one side of the 3×3 cluster and more energy is lost from the opposite side. The effects do not cancel completely and as a result the reconstructed energy decreases, reaching a minimum at the crystal edge. If the impact point is moved further still, the 3×3 cluster is redefined to have the neighbouring crystal at its centre and the reconstructed energy increases. To compensate for this effect, an empirical correction is applied that essentially estimates the point of impact using the distribution of recorded energy within the cluster, and adjusts the total energy accordingly. The distribution of reconstructed energy that is obtained after applying this correction corresponds to the filled histogram of Fig. 6. A Gaussian fit to the central part of the distribution has a standard deviation corresponding to $\sigma_E/E=0.5\%$, fulfilling the design goal. It should be noted that the correction uses only information from the ECAL and can thus be applied to photons as well as electrons.

4.2.1.4. Additional experiment-related factors influencing energy resolution. The preceding discussion concentrated on the performance expected for the Barrel section of the ECAL. The situation in the Endcaps is complicated by the presence of the Preshower detector, needed in this region to improve the discrimination

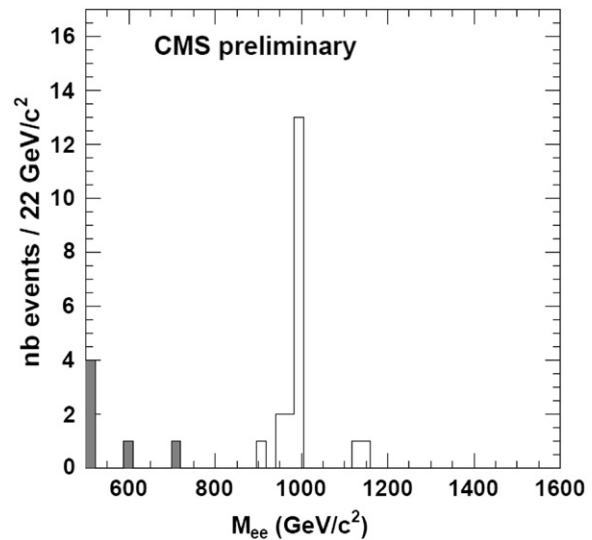


Fig. 7. The open histogram is the reconstructed mass spectrum for a Randall-Sundrum graviton with a mass of 1 TeV and a width of 14 MeV, decaying to an e^+e^- pair. The shaded histogram indicates the expected background.

between single photons and pairs of photons from π^0 decays. The lead converters of the Preshower detector have a total thickness of $3X_0$ and significantly degrade the energy resolution in the crystal calorimeter. This loss in resolution is only partly recovered by including pulseheight information from the silicon sensors in the energy sum. However, kinematic effects associated with the Lorentz boost received by particles traversing Endcaps, allow the primary physics goals to be fulfilled with less demanding requirements for the energy resolution in this region. Thus the stochastic term should have $a \geq 6\%$ (dominated by the effect of the Preshower) and the electronic noise will contribute typically 150 MeV/channel to b (reflecting the lower signal sensitivity of the VPTs compared to the APDs). The aim is to achieve a constant term (the dominant contribution to the energy resolution at high energy) similar to that for the Barrel: $c=0.55\%$.

Another important factor affecting both the Barrel and the Endcap sections of the calorimeter is the presence of the Silicon Tracker, which occupies the central volume of CMS, between the beam pipe and the front surfaces of the ECAL. The material budget of the Tracker and its services amounts to $0.4 X_0$ at the centre of the Barrel section ($\eta=0$), it increases to $1.8 X_0$ at the ends of the Barrel ($\eta=1.5$) and then decreases to $1.0 X_0$ at the inner radius of the Endcaps ($\eta=2.5$).

The effect of the Tracker material, combined with the 3.8 T magnetic field, complicates the energy reconstruction for both electrons and photons. In the case of an electron, radiation of a hard photon can result in an increase in the size of the associated cluster in the ECAL, or even produce a secondary cluster. The reconstruction algorithm is therefore in general more sophisticated than an energy sum over a 3×3 or 5×5 array of crystals. In the case of photons, pair production in the material of the Tracker causes a loss in detection efficiency, but the energy resolution for unconverted photons is not degraded.

Simulated analysis studies have been performed which reproduce as closely as possible the anticipated performance of the ECAL and the other CMS sub-systems under the conditions that will be experienced during operation. A physics channel which relies particularly heavily on information from the ECAL is the production and decay of a hypothetical heavy neutral state decaying into an electron-positron pair. Fig. 7 shows the reconstructed mass peak that would be obtained, within the framework of a particular model, for a state with a mass of 1 TeV. The width

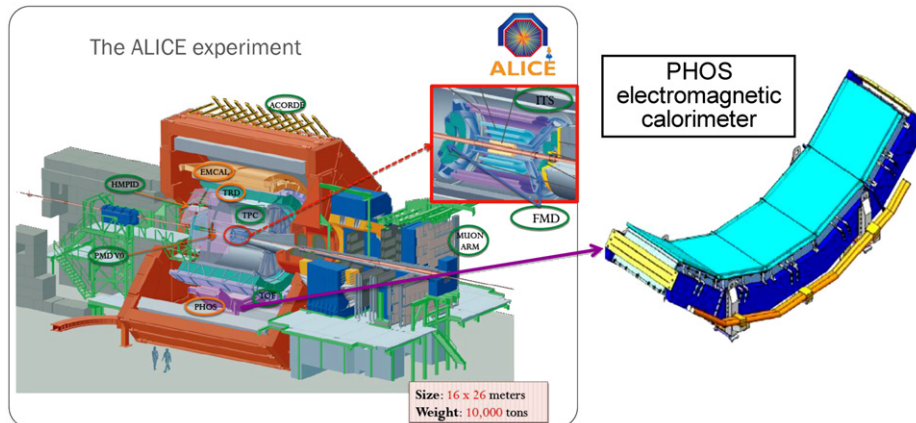


Fig. 8. The ALICE experiment at the LHC, showing the principal detector sub-systems. The PHOS lead tungstate calorimeter is visible near the bottom of the central section of the detector and is shown in enlarged detail on the right.

of the observed peak is entirely dominated by the assumed decay width of 14 GeV, demonstrating the power of the ECAL in measuring high energy electrons.

4.2.2. The ALICE PHOS

Lead tungstate crystals have also been selected as the active medium in a homogeneous electromagnetic calorimeter for ALICE, another of the four major experiments at the LHC. ALICE (A Large Ion Collider Experiment) [16] has as its primary goal the study of strongly interacting matter at extreme densities, produced in high energy collisions of heavy ions, where formation of quark-gluon plasma is expected. ALICE consists of a number of sub-systems, designed to probe a wide range of properties of heavy ion collisions. For example, the PHOS (PHOton Spectrometer) [17] is designed to measure thermal radiated photons to gain information on the temperature of the created medium. It is also used together with the EMCAL (Section 4.3.3) to measure direct photons recoiling against jets.

The thermal photons are expected to be accessible in the energy range 1–10 GeV, thus the PHOS is required to have good energy resolution extending down to a few hundred MeV. A second important requirement is fine transverse segmentation, since the number of tracks produced per unit solid angle in energetic heavy ion collisions is extremely high. On the other hand, the constraints of radiation hardness and high rate capability are less demanding than those influencing the ECAL designs of the two LHC general purpose detectors, ATLAS and CMS. Thus although the basic detection principle – lead tungstate crystals coupled to APDs – is the same as that used for the Barrel of the CMS ECAL, the divergent primary physics goals of the two experiments has led to different implementations.

The ALICE detector (Fig. 8) has two major sections: a central part, immersed in the magnetic field of a large iron-yoke magnet, and a muon arm, visible towards the right of the main figure. The PHOS calorimeter is located towards the bottom of the central section, 460 cm below the interaction region, and is shown in more detail on the right of Fig. 8.

The PHOS covers 100° in azimuth angle (the angle in the plane normal to the beam direction), and extends over the pseudorapidity range ($-0.13 < \eta < +0.13$). It comprises five identical modules, each containing 56×64 crystals and covering 20° in azimuth. There are 17 920 crystals in total, all are identical rectangular parallelepipeds with dimensions $22 \times 22 \times 180$ mm³. The scintillation light is detected with a single APD (Hamamatsu

type S8140), with a sensitive area of 5×5 mm², mounted on the rear face of each crystal and covering 5% of the area.

A notable feature of the PHOS is that it operates at a temperature of -25 °C. This gives an enhancement of approximately a factor of 3 in the crystal light output, compared to that at room temperature, resulting in the release of approximately 4.5 photoelectrons/MeV in the APD. (It may be remarked that low temperature operation was not a practical option for the CMS crystal ECAL, since the radiation levels encountered in CMS are several orders of magnitude higher than those in ALICE and achieving the required degree of radiation hardness in CMS relies on thermal self-annealing of crystal colour centres, which in turn requires operation close to room temperature.)

The APDs are operated at a gain of 50, and each is coupled to a low noise charge-sensitive preamplifier (CSP), located within the -25 °C enclosure. The CSP has a rise time of 15 ns, an RC discharge time of 100 µs, and a sensitivity of 0.833 V/pc. It produces an output voltage step proportional to the input charge, which is processed by a CR-RC2 shaper, mounted on a front-end electronics card operating at room temperature, to produce a semi-Gaussian signal with a 2 µs peaking time. Two gains are provided on each channel to obtain 14 bit dynamic range from a pair of 10 bit ADCs. The electronic noise is 615 electrons, which is equivalent to 3.1 MeV. This excellent value for the single channel noise comes in part from the slow shaping time made possible by the low collision rate (8 kHz) at which ALICE will operate. The resultant noise for a cluster of crystals is ~ 18 MeV.

The first of the five PHOS modules to be completed was tested in a beam at CERN in 2006, at an operating temperature of -17 °C. The energy resolution was measured with electrons over the momentum range 1–5 GeV/c. The results are shown in Fig. 9, where they are compared with earlier measurements made with prototypes over a wider energy range, and with the ALICE design goal, indicated by the solid line. The full set of measurements is well described by a relative energy resolution function, shown as a broken line, of the form:

$$\frac{\sigma(E)}{E} = \frac{3.3\%}{\sqrt{E}} \oplus \frac{1.8\%}{E} \oplus 1.1\% \quad (24)$$

confirming that the design performance will be achieved.

4.2.3. The NA48 liquid krypton calorimeter

Liquefied noble gases have physical characteristics that make them well suited to applications in electromagnetic calorimetry. For example, the high mobility of electrons in these liquids makes possible the measurement of energy loss by ionization through

collection and measurement of the released charge. In addition, they exhibit strong scintillation properties, with light yields comparable to crystal scintillators such as thallium doped sodium iodide ($\text{NaI}[\text{TI}]$). For economic reasons, liquid argon has been the material of choice for very large detectors with liquid krypton and liquid xenon finding application in smaller devices. Some of the properties of these materials, relevant to calorimetry, are given in [Table 2](#).

Of the liquids listed in [Table 2](#), argon has the longest radiation length and has been used in homogeneous detectors that act as both tracking devices and calorimeters, such as the ICARUS time projection chamber [18] located in the Gran Sasso Laboratory. When argon is used for applications focused on calorimetry alone, it is normally in combination with a dense passive absorber such as lead.

In comparison, liquid krypton and liquid xenon have much shorter radiation lengths and are therefore more suitable for use in homogeneous calorimeters. These two liquids have similar Molière radii, thus for a fixed-target accelerator experiment, where the longitudinal space required by the calorimeter is not necessarily a strong constraint, the advantage of xenon, with its shorter radiation length, may be outweighed by its higher cost.

A notable example of a homogeneous ionization calorimeter based on liquid krypton is the device built for the NA48 experiment at the CERN Super Proton Synchrotron (SPS) [19]. The primary aim of NA48 was to study direct CP-violation in the neutral kaon system. This required *inter alia* measurements of the decays of long-lived and short-lived neutral kaons into pairs of neutral pions ($K_L \rightarrow \pi^0\pi^0$, $K_S \rightarrow \pi^0\pi^0$). The four photons resulting from the prompt $\pi^0 \rightarrow \gamma\gamma$ decays (with average energies of 25 GeV) were measured in the electromagnetic calorimeter, which provided precise information on the energies of the

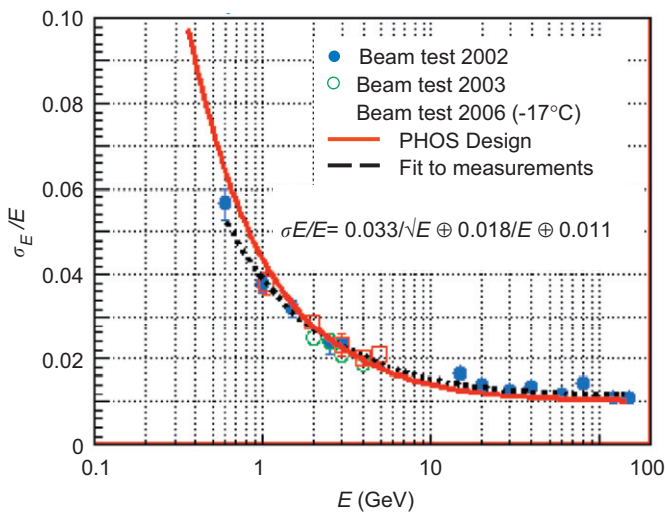


Fig. 9. The relative energy resolution as a function of energy of the PHOS electromagnetic calorimeter of ALICE. The open and filled circles are the results of measurements made on prototypes. The open squares are results obtained with the first complete production module. The dotted line is the result of a fit to all the data. The solid line is the design goal.

photons and the transverse distances of their impact points from the beam axis.

The calorimeter is shown schematically in [Fig. 10a](#). It has a liquid volume of 10 m^3 , with a depth along the beam line of 125 cm ($27X_0$) and an active area of approximately 5.3 m^2 . The neutral beam passes through a 16 cm diameter vacuum pipe, centred on the axis of the calorimeter. The krypton is recirculated and cleaned in an external purifier, giving a free electron lifetime greater than $100 \mu\text{s}$. The electrode structure is shown in [Fig. 10b](#). The anodes and cathodes are ribbons of copper–beryllium alloy, aligned almost parallel to the beam direction. They are not planar,

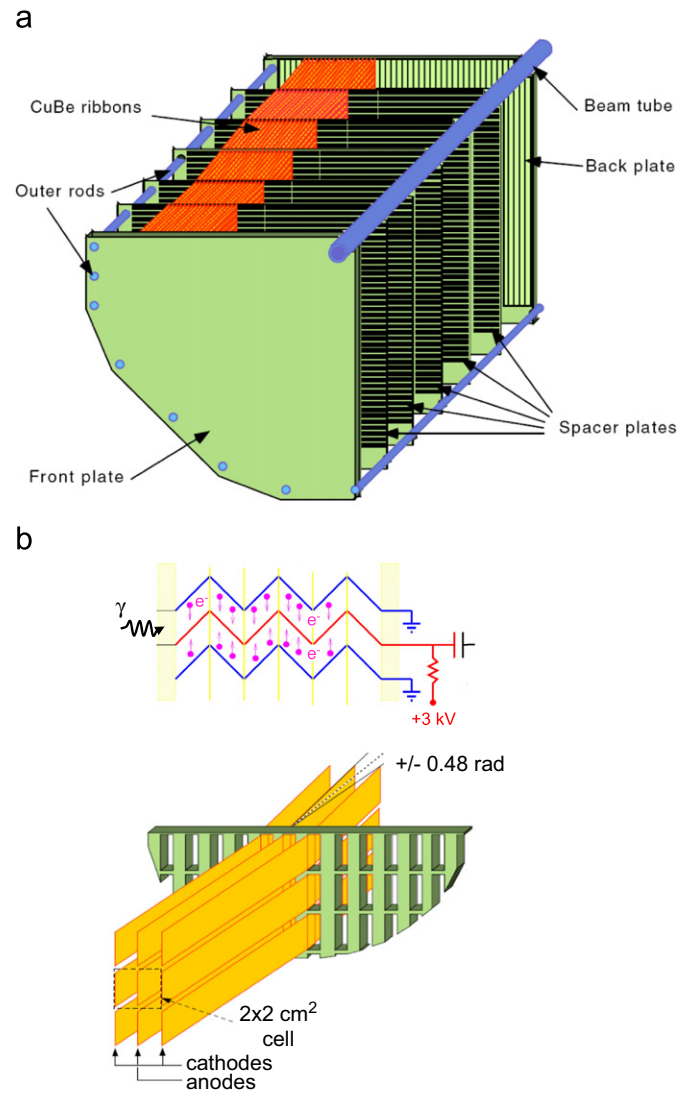


Fig. 10. (a) Schematic view of one quadrant of the NA48 liquid krypton electromagnetic calorimeter. (b) Detailed view of the electrode structure of the liquid krypton calorimeter, together with a sketch indicating the “accordion” folding.

Table 2

Properties of liquefied noble gases. W_i is the energy required to create an electron/ion pair. F is the Fano factor, relevant for detectors measuring ionization. T_{BP} is the boiling point at atmospheric pressure.

Z	A	T_{BP} (K)	Density (g/cm³)	X_0 (cm)	R_M (cm)	E_c (MeV)	dE/dx (min) (MeV/cm)	W_i (eV)	F
Argon	18	39.9	87.3	1.40	14.0	9.0	31.9	2.11	23.6
Krypton	36	83.8	119.9	2.42	4.7	5.9	16.5	3.28	18.4
Xenon	54	131.3	165.1	2.95	2.9	5.2	11.3	3.71	15.6

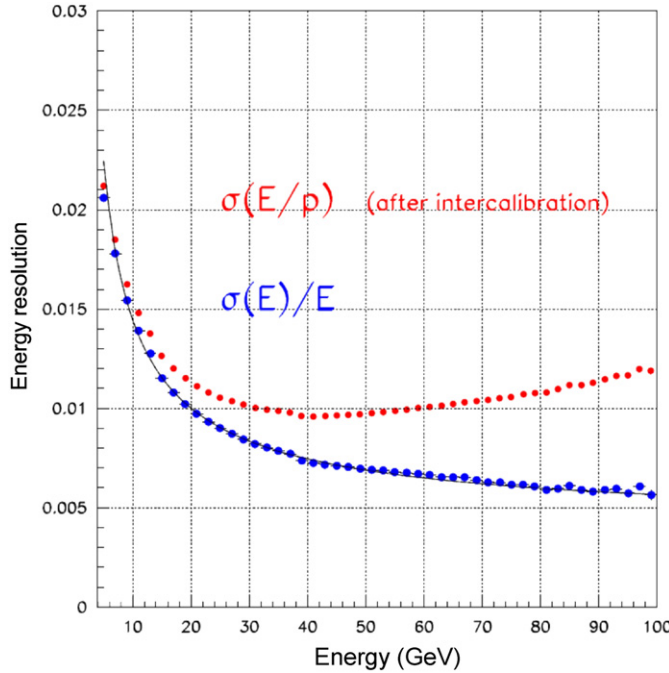


Fig. 11. The energy resolution of the NA48 liquid krypton calorimeter obtained using electrons measured in the magnetic spectrometer. The upper curve includes the spectrometer resolution. The lower curve shows the nett calorimeter resolution after unfolding the spectrometer resolution.

but have a zigzag (accordion) shape to avoid a dependence of the response on transverse position. (This geometrical arrangement was pioneered by the RD3 Collaboration and applied to the lead absorber plates and electrodes of the liquid argon sampling electromagnetic calorimeter of ATLAS, described in Section 4.3.1.) The spacing between electrodes is 1 cm, giving an electron drift time of approximately 3 μ s. The electrodes are arranged to form cells $2 \times 2 \text{ cm}^2$ in cross-section, pointing towards the centre of the kaon decay region, 114 m upstream.

Signals are processed by preamplifiers mounted within the liquid krypton before transmission to transceivers located outside of the cryostat. Fast shaping is performed with a Bessel filter to give a pulse width of 70 ns. A gain switching amplifier, followed by a 10-bit, 40-MHz FADC provides a full scale energy of 55 GeV, with a sensitivity of 3.5 MeV at the highest gain. Since the Molière radius is about three times the cell size, electromagnetic showers spread over a large number of cells. Thus about 100 cells within a radius of 11 cm contribute to the energy summation. The energy resolution as a function of energy was determined using $K_L \rightarrow \pi^\pm e^\pm \nu$ decays. For each event, the electron energy was obtained from a measurement of its momentum in the magnetic spectrometer of the experiment.

The results are shown in Fig. 11. After unfolding the spectrometer resolution, the calorimeter resolution function is well described by the expression:

$$\frac{\sigma(E)}{E} = \frac{(3.2 \pm 0.2)\%}{\sqrt{E}} \oplus \frac{(9 \pm 1)\%}{E} \oplus (0.42 \pm 0.05)\% \quad (25)$$

The position resolution (Fig. 12) was obtained by comparing shower centroids with electron impact points estimated by extrapolating tracks measured in the spectrometer. The resolution improves with increasing energy and is better than 1 mm above 25 GeV.

Having played a major role in enabling the NA48 experiment to reach its physics goals, the LKr calorimeter is currently being upgraded for a new experiment, NA62, due to start in 2011. NA62

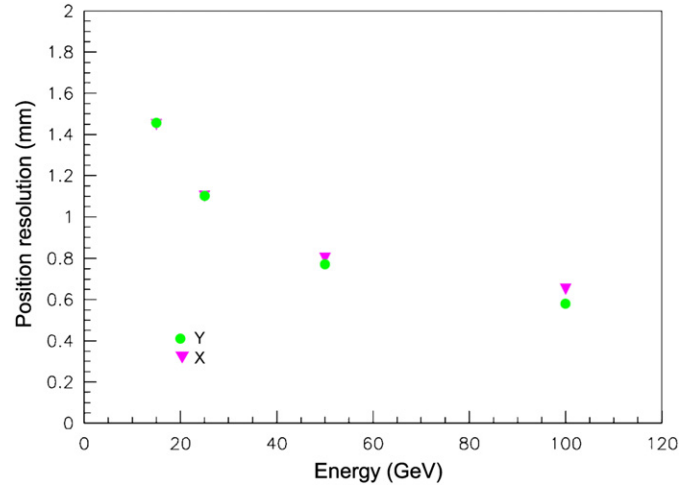


Fig. 12. The position resolution of the liquid krypton calorimeter.

is designed to measure the rare kaon decay $K^+ \rightarrow \pi^+ \nu \bar{\nu}$, which is predicted to have a branching ratio of $\sim 8 \times 10^{-11}$. The LKr calorimeter will be required to veto high energy photons in the energy range 5–50 GeV, with an inefficiency of less than 10^{-5} . This will require the readout rate to be increased from 13 kHz to 1 MHz, while retaining as much of the existing analogue electronics as possible, for reasons of economy. The new system [20] will buffer events during a complete 8 s beam spill and transfer the raw data to a PC farm via Gigabit Ethernet for processing between spills.

4.2.4. The MEG liquid xenon calorimeter

The strong scintillation emission from liquefied noble gases has been exploited in a number of experiments. A good illustrative example is the MEG (Muon to E Gamma) experiment, currently recording data at the Paul Scherrer Institute (PSI) in Switzerland [21], which incorporates a large liquid xenon electromagnetic calorimeter [22].

Scintillation emission from liquefied noble gases arises from the decay of excimers (diatomic molecules, existing only in an excited state) to the dissociative ground state [23]. Ionizing particles produce excimers through two distinct mechanisms: direct atomic excitation and ionization followed by electron-ion recombination. The two lowest excited states of the Xe_2^* excimer are a singlet and a triplet, which decay with time constants of approximately 4 and 20 ns, respectively, making xenon the fastest scintillator among the noble gases. Scintillation initiated by fission fragments is faster than that produced by alpha particles, since the intensity of singlet emission, relative to triplet emission, increases with increasing ionization density. In the case of excitation by relativistic electrons, the emission is somewhat slower and is characterized by an effective time constant of ~ 45 ns. This is attributed to the slower production of excimer states through the electron-ion recombination process dominating the emission time in this case. (It may be noted that the different decay times associated with different ionization densities opens the possibility of discrimination between different types of particle, based on pulse shape. This has been exploited to reject γ -ray backgrounds in liquid xenon detectors used in direct searches for dark matter [24].)

Scintillation emission from xenon is in the vacuum ultraviolet, centred at a wavelength of 178 nm, with a spread of 14 nm (fwhm). Approximately 40 000 photons are emitted per MeV of deposited ionization energy.

MEG searches for the lepton flavour violating decay $\mu^+ \rightarrow e^+ + \gamma$, aiming to reach a sensitivity of 10^{-13} for the decay

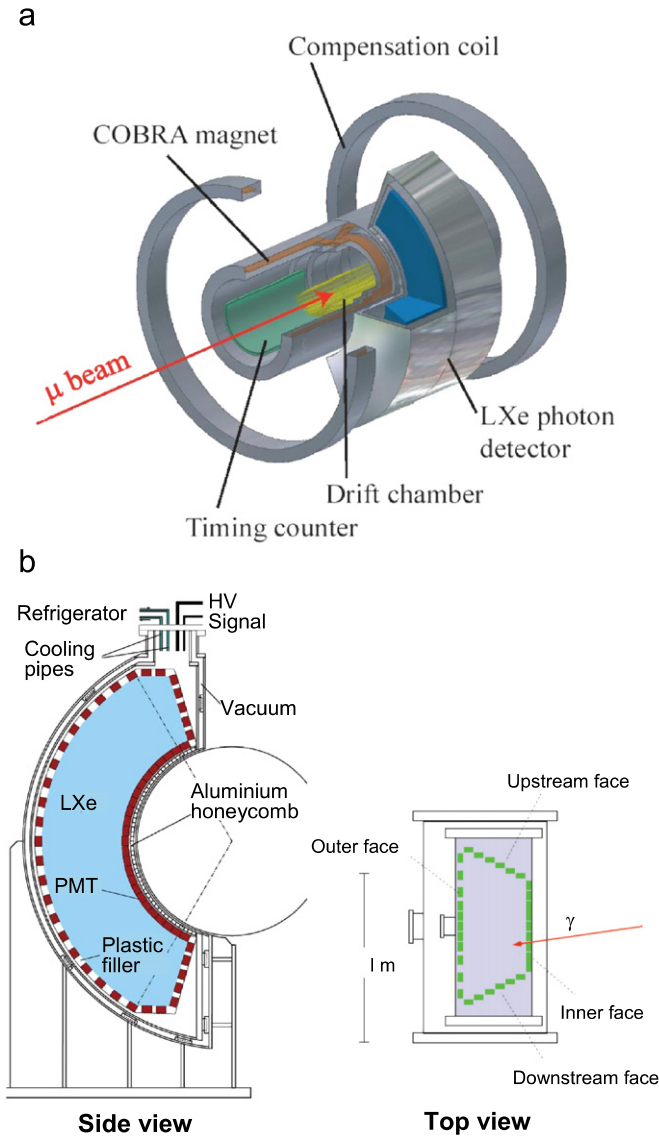


Fig. 13. (a) Layout of the MEG experiment at PSI, showing the COBRA spectrometer and the liquid xenon electromagnetic calorimeter. (b) Detailed views of the electromagnetic calorimeter, in the vertical (left) and horizontal (right) projections.

branching fraction. Detection of a signal at this level would provide an unambiguous indication of physics beyond the Standard Model. A decay $\mu^+ \rightarrow e^+ + \gamma$ at rest is characterized by the back-to-back emission of a positron and a photon, each having an energy close to 52.8 MeV (corresponding to half the muon mass). The dominant background arises from accidental coincidences between positrons from $\mu^+ \rightarrow e^+ + v_e + \bar{v}_\mu$ decays and photons from other processes. Thus a key requirement in achieving the experiment goal is a precise measurement of the energy, impact point and timing of 50 MeV photons.

The layout of the experiment is shown in Fig. 13a. Positrons are measured in a magnetic spectrometer ("COBRA") consisting of a thin-walled superconducting magnet and a set of low-mass drift chambers. The electromagnetic calorimeter (Fig. 13b) has an 800 l, c-shaped active volume, with inner and outer radii of 65 and 112 cm, respectively, giving a depth of liquid xenon corresponding to $17X_0$. It covers an angular range of 120° in the vertical plane and approximately $\pm 25^\circ$ along the direction parallel to the beam, giving a solid angle coverage of 10%. The steel cryostat has a thin (0.5 mm) steel window at the front, supported by an

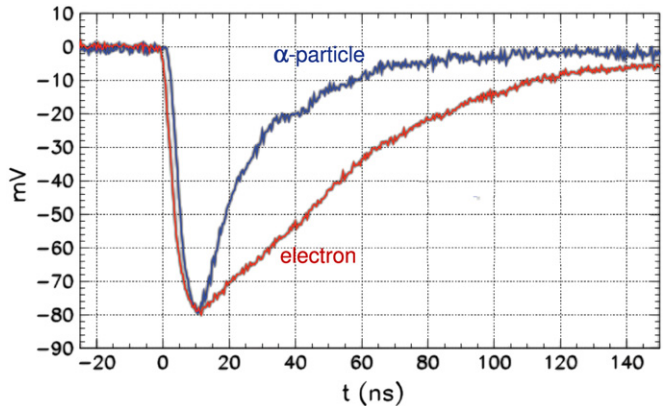


Fig. 14. Scintillation pulse shape in liquid Xe obtained with excitation by high energy electrons and alpha particles.

aluminium honeycomb, to minimize the amount of inert material between the muon stopping target and the liquid xenon. Scintillation light is detected with a set of 846 2 in., UV-sensitive phototubes, immersed in the liquid xenon.

Two types of digitizer process the signals from the phototubes. One operates at 100 MHz and generates information for the trigger. The other system employs the DRS (Domino Ring Sampler) ASIC developed at PSI, which provides each channel with a circular pipeline of 1024 capacitors, sampled at 2 GHz to give 40 ps timing resolution. Pulse shape distributions obtained with alpha particles and with electrons are shown in Fig. 14. They demonstrate the strong dependence of the scintillation characteristics of liquid xenon on the type of ionizing particle.

Several calibration and monitoring strategies are used to ensure that the optimum performance of the calorimeter is achieved and maintained during running. The performance of the photomultipliers is checked with light emitting diodes and with ^{241}Am alpha sources mounted on tungsten wires within the xenon. A 1 MeV Cockcroft-Walton proton accelerator provides a precise and fast method of calibrating the calorimeter using 14.8 and 17.6 MeV γ -ray lines produced in the $^7\text{Li}(p,\gamma)^8\text{Be}$ reaction. In addition, the $^{11}\text{B}(p,\gamma)^{12}\text{Be}$ reaction, leading to the simultaneous emission of two photons (4.4 and 11.7 MeV), is used to study the relative timing of signals from the calorimeter and a timing counter.

Finally, the charge exchange reaction, $\pi^- + p \rightarrow \pi^0 (\rightarrow 2\gamma) + n$, initiated by negative pions stopping in a liquid hydrogen target, provides a powerful method of studying the energy resolution, energy scale and spatial resolution of the calorimeter at photon energies relevant to the rare decay search. There is a correlation between the energies of the two photons from the π^0 decay and the opening angle between them, resulting in a flat spectrum from 54.9 to 82.9 MeV, with the limiting energies corresponding to an opening angle of 180° . Such pairs of back-to-back photons are selected with a NaI tagging detector mounted on the side of the target opposite to the calorimeter and moved to scan the full acceptance of the calorimeter. An energy distribution obtained with 55 MeV photons is shown in Fig. 15. The peak is asymmetric, with a tail on the low energy side associated with photons converting in front of the sensitive volume. The line shape also depends to some extent on the depth of photon conversions within the liquid xenon. For conversions occurring at depths greater than 2 cm, the average resolution is $\Delta E/E = (5.8 \pm 0.35)\%$ (fwhm). The shape of the high energy side of the distribution is particularly important, since it influences the probability for low energy background photons to be shifted into the signal region. A Gaussian fit to the upper half of the peak yields $\sigma_{upper} = (2.0 \pm 0.15)\%$,

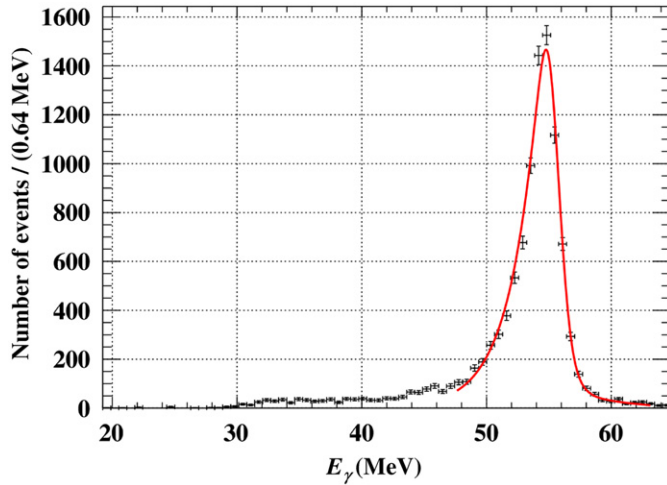


Fig. 15. Energy distribution obtained with 55 MeV photons from the charge exchange reaction: $\pi^- + p \rightarrow \pi^0 + n$.

where the quoted error includes variations over the calorimeter acceptance.

The spatial resolution, obtained by studying the shadow of a lead collimator, is 15.0 mm (fwhm), and the timing resolution is found to be 150 ps (fwhm).

Fig. 15 clearly demonstrates the power of the liquid xenon technique for measuring photons with energies of a few tens of MeV. The high light-yield and long attenuation length of liquid xenon makes it possible to keep the contributions to the energy resolution function from the stochastic and noise terms very small. For comparison, the CMS and NA48 calorimeters would have a stochastic term of $\sim 15\%$ at 50 MeV (although in practice, readout noise would dominate the resolution function at this energy).

4.3. Sampling calorimeters

Sampling devices offer the potential advantages of very fine granularity and containment of electromagnetic showers in situations where space is restricted. Depending on the technology chosen and the details of the design, sampling devices can also provide the most cost effective solution for some applications. An important challenge to be overcome in the construction of large scale detectors is achieving the tight mechanical tolerances required for high resolution and good uniformity of response.

4.3.1. The ATLAS liquid argon ACCORDION sampling calorimeter

4.3.1.1. General description. ATLAS (A Toroidal LHC ApparatuS) [25] is an LHC general purpose detector. Its aim is to cover the same wide range of discovery physics as CMS, but it has placed different relative priorities on some types of particle measurement, resulting in a rather different overall design philosophy. The very high energies, luminosities and radiation levels at the LHC pose particular challenges for the detector systems. In order to meet these challenges ATLAS has chosen a highly granular lead/liquid argon (LAr) sampling electromagnetic calorimeter covering the pseudorapidity range $|\eta| < 3.2$. The design has been guided by the benchmark process of a Higgs boson decay to two photons, for $M_H < 150 \text{ GeV}/c^2$. To discover such physics the calorimeter must have excellent photon resolution, with uniform photon measurement and good γ/π^0 discrimination across the entire calorimeter. The search for Higgs decays to final states containing several electrons (for example $H \rightarrow ZZ \rightarrow e^+e^-e^+e^-$) requires measurements over a large range of electron energies. High precision measurements of the W boson mass, at the sub % level,

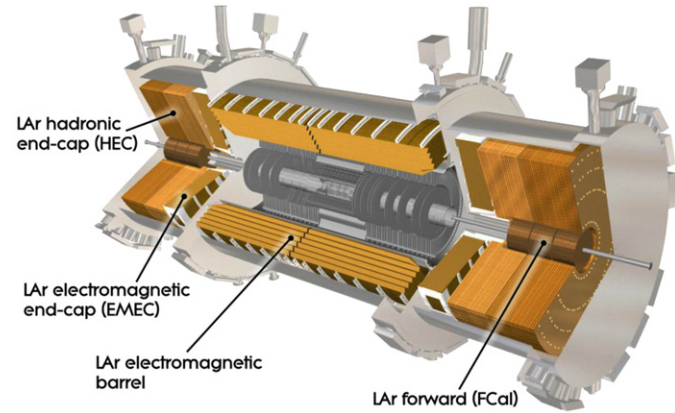


Fig. 16. Schematic layout of the ATLAS liquid argon calorimeters.

place further emphasis on detector uniformity. With these considerations in mind, ATLAS set stringent design goals for the terms governing energy resolution (Eq. (14)), requiring the stochastic term, a , to be no greater than $10\%/\sqrt{(E/\text{GeV})}$ and the constant term, c , to be below 0.7%. The design is based on a novel arrangement of the absorber plates and electrodes which are arranged with the ‘accordion’ geometry, developed by the RD3 collaboration [26]. The calorimeter is one of the largest and most powerful sampling electromagnetic calorimeters built for high energy physics, with a total of $\sim 174,000$ readout channels.

It comprises a Barrel section, made of two halves, together covering the central pseudorapidity range, $-1.475 < \eta < 1.475$ and two Endcaps, each covering a region $1.475 < |\eta| < 3.2$ (Fig. 16). In addition, there is a ‘forward’ combined electromagnetic/hadronic liquid argon calorimeter at each end, covering the region $3.2 < |\eta| < 4.9$. The Barrel calorimeter is located behind the superconducting coil, within the solenoid cryostat. Each Endcap calorimeter is enclosed in a cryostat which it shares with the Hadron Endcap calorimeter and with the Forward calorimeter. The Barrel is 640 cm long and 53 cm deep, with an inner radius of 140 cm, and weighs 114 t. The Endcaps are 63.2 cm thick and extend from 30 to 200 cm in radial distance from the beam. Each weighs 27 t. In front of the Barrel and part of the Endcaps, for $|\eta| < 1.8$, there is a 10 mm thick ‘presampler’ to provide an estimation of energy lost upstream of the calorimeter. In the Barrel region, the material budget in front of the detector, associated with the solenoid and the tracker, varies from $\sim 2X_0$ at $\eta=0$ to $5-6X_0$ for η from 1.5 to 1.8. In the Endcaps the material budget is $\sim 2.3X_0$.

ATLAS has chosen liquid argon calorimetry because it offers an intrinsically linear response which is stable over time and tolerant to high levels of radiation. The accordion geometry provides high granularity and good hermiticity. The readout is at the front and back of the calorimeter, rather than at the sides, which means that adjacent modules can be tightly packed, with full ϕ coverage and no cracks between modules. A photograph of a Barrel sector of the calorimeter is shown in Fig. 17, together with a close-up view of the assembly, an electrode etched with a pattern to form readout cells, and a simulation of an electromagnetic shower propagating through the calorimeter.

The absorber comprises corrugated lead sheets, 1.53 mm thick (1.13 mm thick for $|\eta| > 0.8$), clad with 0.2 mm thick stainless steel for structural rigidity. A honeycomb spacer sets a gap of 2.1 mm for the liquid argon. This is followed by a corrugated copper-clad kapton electrode sheet and a further 2.1 mm spacer before the next layer of absorber. The electrode comprises three layers, the two outer layers providing high voltage to establish an electric drift field in the gap, and a central electrode for reading

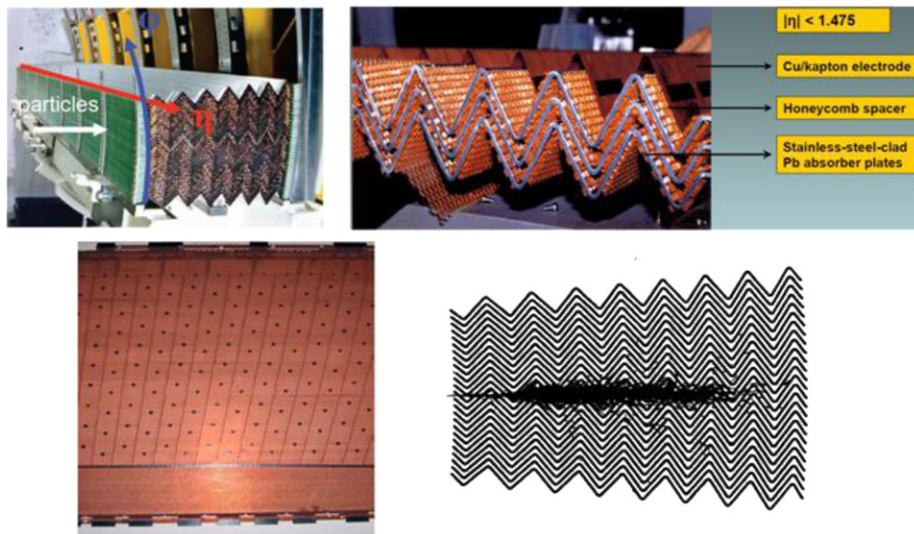
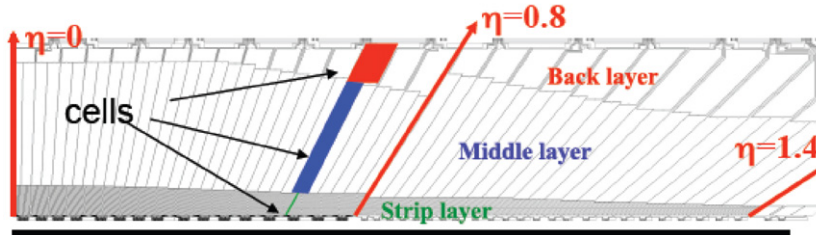


Fig. 17. A section of the Barrel accordion calorimeter (top left); a close-up showing the consecutive layers of absorber, liquid argon drift space, spacers and electrodes (top right); an electrode etched to form the readout cells (bottom left); a simulation of an electromagnetic shower as it propagates through the absorbers (bottom right).



Layer	Function	Size ($\Delta\eta \times \Delta\phi$)
0 = Presampler	Estimates energy loss before calorimeter	0.025 × 0.1
1 = Strips	High granularity for π^0/γ discrimination	0.003 × 0.1 ($\eta < 1.4$)
2 = Middle	Contains bulk of em shower energy	0.025 × 0.025
3 = Back	Tail of em shower, hadron shower rejection	0.05 × 0.025

Fig. 18. The layout of the cells on the readout electrodes for a Barrel section of the ATLAS LAr electromagnetic calorimeter.

out the signal. The signal arises from the movement, in the electric field, of the electrons released by ionization from the electromagnetic shower in the liquid argon. The signal is read out on the central electrode through capacitive coupling with the high voltage electrodes which collect the charge. The total drift time is ~ 450 ns at an operating voltage of 2000 V. The Barrel section comprises 1024 absorbers arranged into two half-barrels, each containing 16 modules. Each Endcap consists of an inner and outer wheel with 256 and 768 absorbers, respectively. The drift gaps between the Endcap absorbers increase with radius. To compensate for the longer drift distances, the high voltage is increased in steps in order to achieve similar drift times.

The total thickness traversed by a particle passing through the calorimeters varies from $22X_0$ to $30X_0$ in the pseudorapidity range $0 < |\eta| < 0.8$, and from $24X_0$ to $33X_0$ in the range $0.8 < |\eta| < 1.3$. This provides sufficient containment of the electromagnetic shower to ensure high energy resolution, as illustrated by the simulation of a shower in Fig. 17 (bottom right). In the Endcaps, the depth increases from 24 to $38X_0$ in the range $1.475 < |\eta| < 2.5$, and from 26 to $36X_0$ in the range $2.5 < |\eta| < 3.2$.

The high granularity of the accordion calorimeter is achieved by etching the copper electrodes to form areas with the required geometric layout (Fig. 17, bottom left). The areas of etched electrode

are arranged to point towards the interaction point and are split into a strip layer of high granularity for γ/π^0 discrimination, a middle layer to measure the bulk of the electromagnetic shower energy and a back section for hadron shower rejection.

Sets of electrodes, from adjacent calorimeter gaps, are grouped together using passive summing boards located at the front and rear of the detector. The summing board outputs are connected to motherboards which route the outputs from a specific region to the readout cables. The grouping of electrodes into cells in the Barrel section is shown in Figs. 18 and 19. In the strip layer (sampling 1), narrow cells are formed from 16 summed electrodes in ϕ with a width in η of 4.69 mm (at $\eta=0$), for π^0/γ discrimination. Behind, in sampling 2, the middle section, cells are formed from the summing of 4 adjacent electrodes in ϕ to give cells of 0.025×0.025 in ϕ and η . In sampling 3, the back section, the cell size is 0.025×0.05 . All layers go into the trigger sum. The Preshower, strips, middle and back sections are grouped into trigger towers, covering ranges of 0.1 and 0.0982 in η and ϕ . Similar arrangements are made in the Endcap.

The readout of the cells is through preamplifiers located outside the cryostats at distances of up to 4 m. In order to deal with the 25 ns bunch spacing of the LHC, the shaping amplifiers have a shaping time of 15 ns, with the Presampler and strip sections read

out on 25Ω cable, and the middle and back sections with 50Ω cable. This arrangement optimizes the matching to the respective cathode capacitances. Because of the high frequency at which the readout operates, the cable behaves like a transmission line and its capacitance contributes little to the total electronics noise.

4.3.1.2. Expected energy resolution. Two of the most crucial aspects governing the energy resolution of a sampling calorimeter are the sampling fraction (Eq. (21)) and the uniformity of construction throughout the detector volume. The ATLAS design, using thin lead absorber sheets, ensures that sampling fluctuations are at the level of $10\%/\sqrt{E(\text{GeV})}$. In the Barrel, the ‘peaks’ and ‘troughs’ of the corrugations are aligned along the z direction (parallel to the beam). As a consequence, a particle crosses the corrugations at an angle that decreases with increasing $|\eta|$, with the result that the effective lead absorber thickness varies as $2.1 \text{ mm}/\cos(\theta)$, where θ is the angle of the particle with respect to the beam direction. This causes the sampling fraction to decrease, potentially leading to a loss in resolution (Eq. (21)). To compensate for this effect, the thickness of the lead is reduced from 2.1 to 1 mm beyond $|\eta|=0.8$. A similar optimization has been made in the Endcaps, where the corrugated sheets lie perpendicular to the z direction, and are arranged like the spokes of a bicycle wheel. Thus the absorber thickness changes from 1.7 mm thick for $1.475 < |\eta| < 2.5$ to 2.2 mm thick for $2.5 < |\eta| < 3.2$.

The uniformity of response of the calorimeter is sensitive to variations in the thickness of the lead sheets. A local 1% increase in thickness would lead to a 0.5% reduction in response. The thickness of the lead sheets was tightly controlled at a level of $6.6 \mu\text{m}$ (rms) for the entire production, limiting the estimated impact on the constant term to less than 0.19%. The absorber and sampling gap thicknesses were also monitored, leading to estimated contributions to the constant term of 0.07% and 0.16%, respectively. Together, the contribution from these three mechanical sources is much smaller than the design aim of less than 0.7% for the overall value of the constant term.

4.3.1.3. Measured energy resolution and response uniformity. The energy deposited in the calorimeter is reconstructed by summing

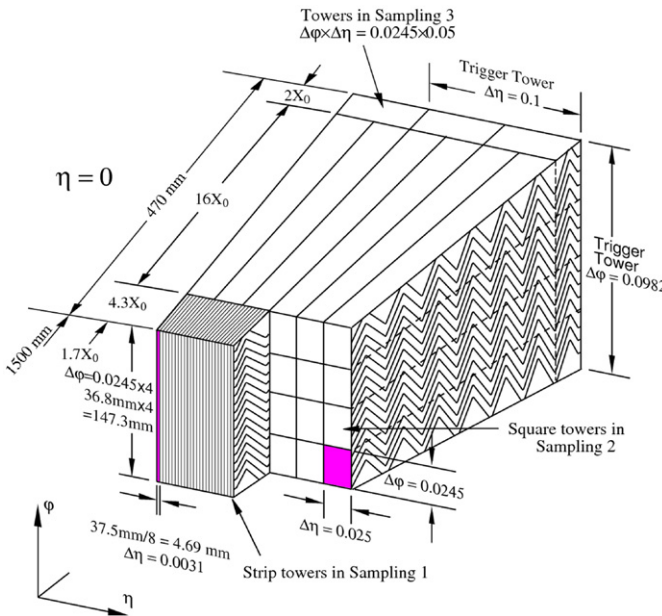


Fig. 19. The grouping of ATLAS Barrel LAr electromagnetic calorimeter cells into readout towers. The fine granularity of the strip towers in Sampling 1 improves γ/π^0 discrimination.

the calibrated cell energies in the three sampling layers: the strip layer, the middle and back layers, together with the energy in the Presampler (Figs. 18 and 19) for a cluster of cells built around the cell with the largest energy deposit in the middle layer. For the test beam analysis, this cluster was a 3×3 group of middle cells centred on the cell with highest response. This choice of cluster size results from striking a balance between the total noise, which increases as the number of cells in the energy sum is increased, and lateral leakage of shower energy, which decreases with increasing cluster size. The fraction of the total electromagnetic energy collected within such clusters is more than 90%.

The relative energy resolution as a function of energy has been measured for a set of Barrel modules in a test beam, with electrons in the energy range 10–245 GeV. The results for particular regions of the calorimeter are shown in Fig. 20, where the experimental measurements, after electronic noise subtraction, have been fitted with the expression $\sigma_E/E = a/\sqrt{E(\text{GeV})} + c$, where a is the stochastic term and c the local constant term. The fit yields a stochastic term of $(10.1 \pm 0.1)\%$ and a constant term of $(0.17 \pm 0.04)\%$, which satisfy the calorimeter design specification.

The mean energy response to 245 GeV electrons, for specific ϕ locations in three Barrel modules, shows an average response uniformity of 0.44% (Fig. 21, left) and an average peak resolution of 0.77% (Fig. 21, right). The change in resolution at η index of 30 reflects the change in Barrel absorber thickness.

The result of extensive measurements at test beams has shown that for the Barrel and Endcap sections of the calorimeter the non-uniformities do not exceed 0.7% and constant terms derived from the energy resolution curves range between 0.5% and 0.7%, which is within the calorimeter design specifications [27].

The power of the electromagnetic calorimeter to provide evidence for new physics is illustrated by Fig. 22, which shows the signal expected from a Randall–Sundrum graviton with a mass of 1.5 TeV decaying into an electron positron pair.

4.3.2. The LHCb electromagnetic calorimeter

LHCb [29] is a specialised experiment at the LHC, dedicated to the study of heavy flavour physics. Its primary goal is to look for

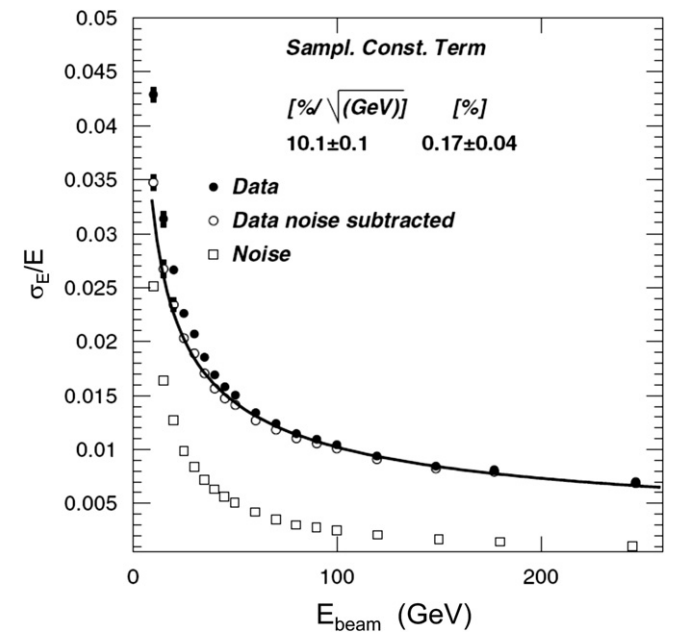


Fig. 20. The relative energy resolution for a particular cell of the ATLAS Barrel LAr electromagnetic calorimeter as a function of electron beam energy, measured in a test beam.

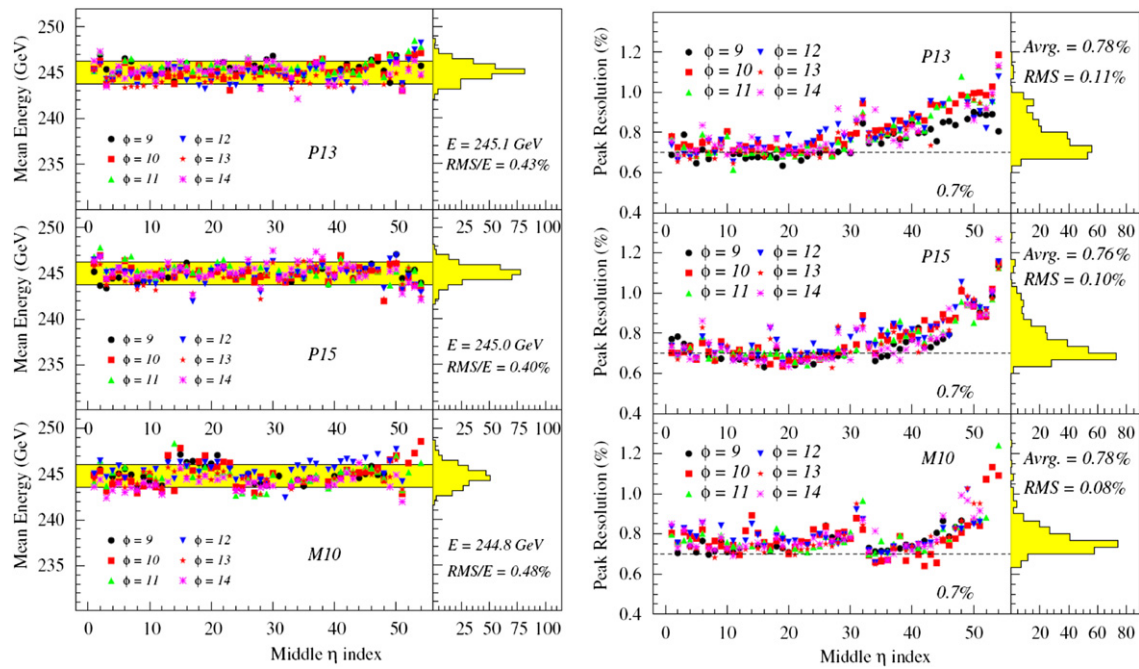


Fig. 21. The mean energy response (left) and relative peak energy resolution (right) at 244.8 GeV, for specific η locations in three Barrel modules of the ATLAS LAr electromagnetic calorimeter, as a function of the middle cell η index.

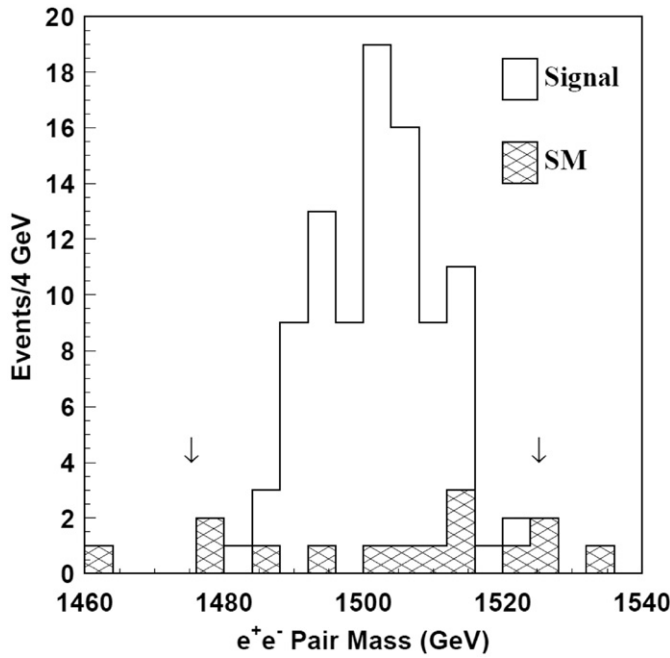


Fig. 22. A simulation of an e^+e^- effective mass distribution in ATLAS, showing the signal expected for a graviton resonance with a mass of 1.5 TeV, superimposed on the expected Standard Model background (SM) for 100 fb^{-1} of integrated luminosity. The mass window used to select the signal is indicated by arrows (taken from [28]).

indirect evidence of new physics in CP violation and rare decays of beauty and charm hadrons. The detector is a forward single-arm spectrometer, designed to collect data at a very high rate in the challenging LHC environment. The calorimeters are required to identify and measure photons, electrons and hadrons and to provide an essential part of the LHCb trigger. Examples of decays which require precise measurements of photon directions and energies are $B_s^0 \rightarrow \phi\gamma$ and $B_d^0 \rightarrow \pi^+\pi^-\pi^0$. The former is particularly

sensitive to new physics, since CP violation should be very small in this channel; the latter provides a complementary channel to $B_d^0 \rightarrow \pi^+\pi^-$, for the determination of the angle α of the unitarity triangle.

For the electromagnetic calorimeter, LHCb has chosen a sampling design [30] which closely follows the "shashlik" format developed over the past 25 years for HERA-B at DESY, DELPHI at CERN and PHENIX at BNL [31]. This decision was made taking into account the requirements for modest energy resolution, fast time response, acceptable radiation resistance and reliability. The detector is cost effective, an important consideration especially for large scale applications such as this. The calorimeter is preceded by a wall of scintillating pads to tag charged particles, and a preshower detector, to improve e/π separation and to tag electromagnetic candidates, located behind $2.5X_0$ of lead. The preshower detector also provides fast particle-identification to the LHCb trigger system.

The design goal of the electromagnetic calorimeter is to achieve an energy resolution characterized by a stochastic term of 10% and a constant term of 1%. It must withstand high radiation doses which, for detector elements near the beam pipe, reach 2.5 kGy per annum at the position of the shower maximum. The transverse segmentation must be adapted to the particle flux as a function of radial distance from the beam and must be small enough to allow the pairs of photons from π^0 decays to be separated, and to minimize effects of pile-up.

The electromagnetic calorimeter (Fig. 23) comprises a wall of 3312 shashlik modules covering a total area of $7.8 \times 6.34 \text{ m}^2$ at 12.5 m from the interaction point. The modules have lateral dimensions of $12.2 \times 12.2 \text{ cm}^2$. The wall comprises an inner, middle and outer region, containing 176, 448 and 2688 modules, respectively. The inner modules are subdivided transversely into 9 cells, each with transverse dimensions $4 \times 4 \text{ cm}^2$, and the middle modules into 4 cells, each $6 \times 6 \text{ cm}^2$. The finer detector granularity in these regions is to improve the separation of the photons from π^0 decays which becomes increasingly difficult close to the beam pipe. The outer modules are not subdivided. The total number of cells that are read out is 6016.

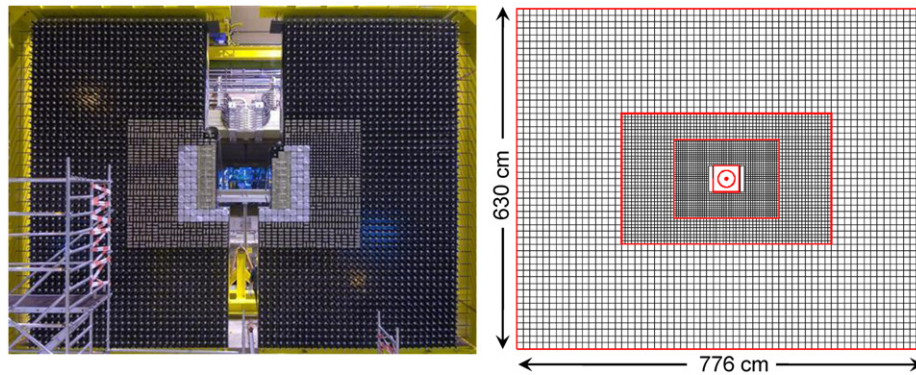


Fig. 23. The electromagnetic calorimeter wall of shashlik sampling modules, looking upstream, under assembly in the LHCb cavern, and a diagram showing the subdivision of the wall (with the cross-hatching) into inner, middle and outer modules. The beam pipe passes through the centre.

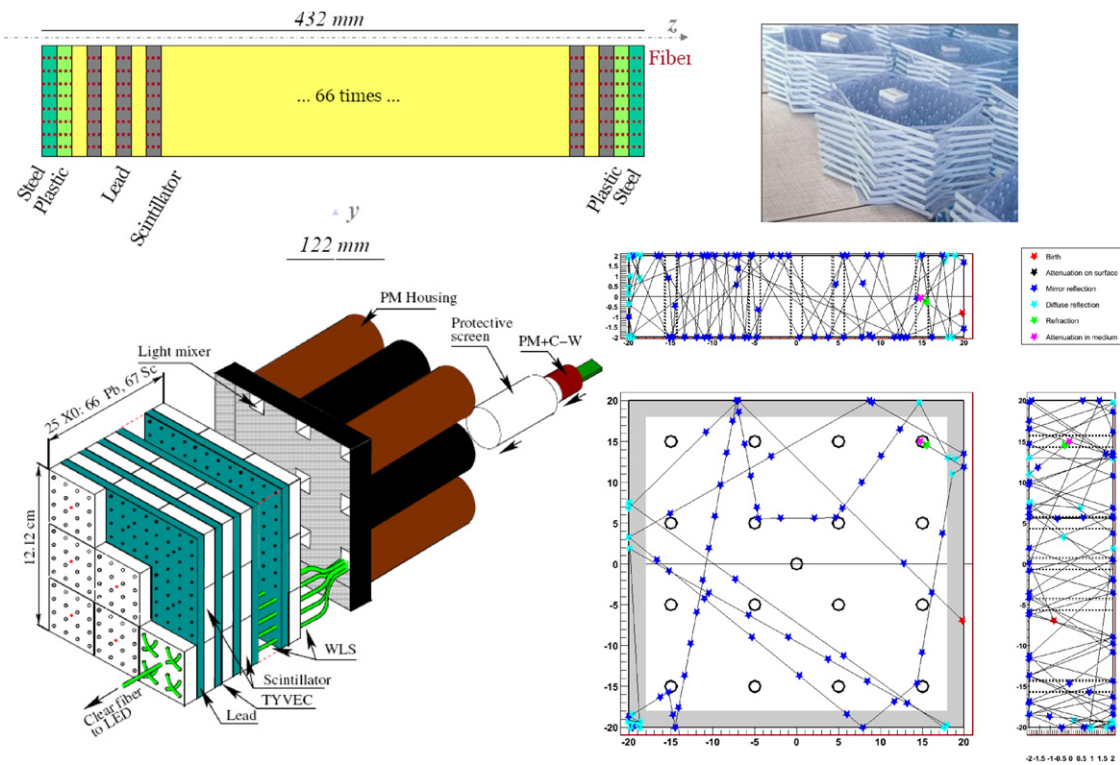


Fig. 24. A drawing showing the assembly of a shashlik module for LHCb and a photograph of a set of scintillator tiles with holes for the passage of the wavelength shifting fibres (top), a schematic of an inner module with 9 cells (bottom left) and an example of a ray tracing simulation of the scintillation light in one of the $4 \times 4 \text{ cm}^2$ tile cells (bottom right).

A shashlik module (Fig. 24) is 42 cm deep and comprises 67 scintillator tiles, each 4 mm thick, interleaved with 66 lead plates, each of thickness 2 mm. This arrangement provides a good balance between the electromagnetic sampling fraction, detector complexity and overall length. The modules have an effective depth of $25X_0$ and a Molière radius of 3.5 cm. Wavelength shifting (WLS) fibres of 1.2 mm diameter pass longitudinally through all the layers. They are looped at the front of the module and pass back to the rear of the module where the ends are collected on to a phototube. In the inner modules, the scintillator planes are comprised of 9 optically decoupled tiles (Fig. 24, bottom left). The WLS fibres pass through the decoupled tiles and are fed to separate phototubes. In the middle modules, each scintillator plane has 4 optically decoupled tiles. The outer modules have single decoupled tiles. The WLS fibres are pitched at 10.1 mm intervals in the inner and middle modules, and at 15.25 mm

in the outer modules. The number of fibres entering the phototube from each cell is 16, 36 and 64, for the inner, middle and outer modules respectively. The respective photoelectron yields from the cells, per GeV of deposited energy, are 3100, 3500 and 2570. The somewhat lower figure for the outer modules is associated with the lower fibre density used for these cells. A completed set of inner, middle and outer modules is shown in Fig. 25.

The scintillation light generated in the tiles by ionizing particles, is internally reflected at the surfaces of the tiles. A fraction of this light, amounting to a few percent, is absorbed by the WLS fibres. This results in the re-emission of light at longer wavelengths, which propagates within the WLS fibres to a phototube. Fig. 24 (bottom right) shows a ray-tracing simulation, following the propagation of scintillation light generated in a tile, and its eventual collection at a WLS fibre. The spread in light yield from tile to tile, which

contributes to the constant term of the energy resolution function, was measured during production and found to be less than 2.5% rms.

A previous limitation of the shashlik design has been the decrease in response that occurs near the boundaries of each module and in the ~0.2 mm thickness of inert material between modules. An innovation introduced by LHCb is the use of a special chemical treatment on the tile edges to produce a diffuse reflection of the scintillation light, giving a relative increase in light collection near the edges and a consequent improvement in response uniformity. However, this technique results in a light yield that is about 30% less than that obtained from tiles with mirrored edges.

The phototube signals are fast, with a rise time of less than 6 ns, making it possible to reduce pile-up by discriminating between events from adjacent bunch crossings of the LHC. The pulses are therefore shaped using a clipping line to eliminate the small tail of pulses extending beyond 25 ns. The resulting pulse has a width of 10 ns (fwhm). The signals are digitized at 40 MHz with a 12-bit ADC. In order to reduce the possible effect of low frequency pickup noise, which would cause a slow variation of the ADC pedestal, a “digital differentiation” is made by subtracting the digitization in a preceding sample (25 ns earlier). To reduce the possibility of subtracting a real signal present in preceding bunch crossing, the quantity subtracted is actually the smallest of the two preceding measurements. Even at the highest occupancy, about 5%, the probability of subtracting a real signal is therefore reduced to less than 0.25%. The electronic noise is less than 1 ADC count and has a negligible impact on the energy resolution.



Fig. 25. Completed inner, middle and outer modules of the LHCb shashlik electromagnetic calorimeter.

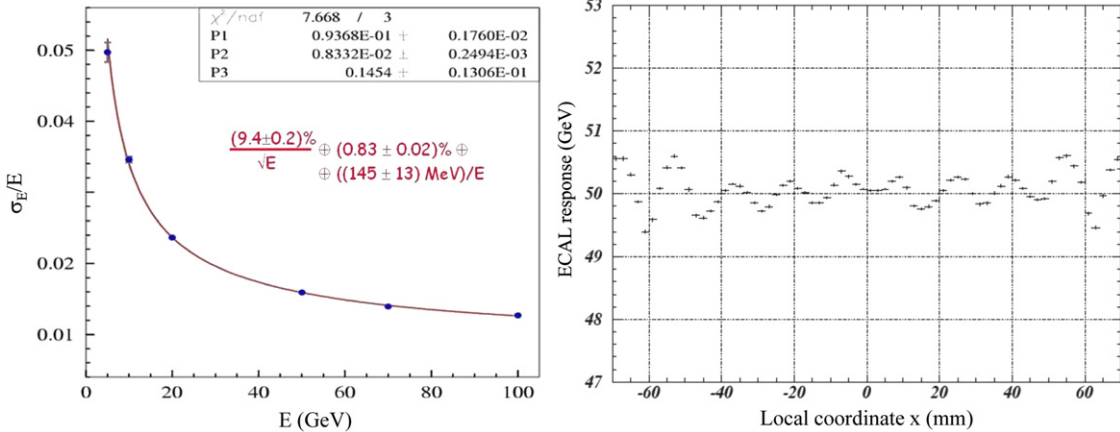


Fig. 26. Results from measurements made on an outer module of the LHCb electromagnetic calorimeter at an electron test beam. Left, the relative energy resolution as a function of energy. Right, the uniformity of response across the module, for beam at normal incidence.

Precise monitoring of the performance of each module, which will be required to follow effects due to radiation damage or changes in phototube response over the 10 years of detector operation, is achieved with a system of light emitting diodes that injects light to all layers of each cell through centrally placed monitoring fibres.

The energy resolution of an outer module has been measured with electrons at a test beam (Fig. 26). The stochastic term and constant term are 9.4% and 0.83%, respectively, meeting the design targets. A lateral scan across the face of the module with a 50 GeV electron beam shows a global non-uniformity of 1.3%, partly caused by imperfect light reflection from the tile edges. Variations at the edge of the module, at ± 60 mm on the plot, correspond to the transition between modules. Local non-uniformities across the inner region, arising from a dependence of the light collection efficiency on the position of the shower with respect to the WLS fibres, are $\sim 0.5\%$. In the experiment, where particles enter at an angle to the calorimeter, non-uniformities are reduced to $\pm 0.6\%$ over the module surface.

4.3.3. The ALICE EMCAL

In addition to the PHOS (Section 4.2.2), the ALICE heavy ion experiment at the LHC has another major subsystem dedicated to the measurement of high energy electrons and photons, the “EMCAL” [32]. The role of the EMCAL is complementary to that of the PHOS, and the different performance requirements have led to different choices of technology. Whereas the PHOS focuses on measuring single photons, the EMCAL concentrates on studying partons produced in the dense hadronic medium generated in high energy heavy ion collisions. Before fragmenting to produce jets of hadrons, the partons will lose energy through gluon radiation and scattering within the hadronic medium. This leads to “jet quenching” by an amount that depends strongly on the density of the medium, resulting in a displacement of jet energies to lower values, the suppression of hadrons with high transverse momentum, and an enhancement in the multiplicity of soft jets.

The measurements of jet quenching effects are complicated by a potential bias arising from jets that have not interacted significantly in the medium. A possible way of overcoming this difficulty is to require the partons to be produced in association with a direct photon recoiling in the opposite direction (Fig. 27).

The photon, which does not carry colour charge, does not interact strongly within the hadronic medium and thus provides a measurement of the parton initial energy. The jets will be measured using information from the EMCAL and from the Time Projection Chamber (TPC), which measures charged tracks. The

recoiling direct photons are measured in the PHOS, which is located in a position diametrically opposite to the EMCAL (Fig. 8 left, and Fig. 28 left). Particle flow studies, such as those described in Section 4.4, show that for ALICE, a hadron calorimeter is not required to make the relevant jet measurements. In the very high multiplicity environment of heavy ion collisions, the jet resolution achieved by combining the excellent charged particle tracking capability of the TPC with the EMCAL measurements would not be improved by adding information from a hadron calorimeter.

The EMCAL is required to measure electromagnetic showers with energies up to ~ 250 GeV and to contribute to the measurement of jets with energies exceeding 200 GeV. In addition to probing jet quenching, EMCAL measurements of high p_T photons, neutral hadrons and electrons will be important for heavy-flavour tagging of jets. The EMCAL also makes a crucial contribution to the fast trigger providing an efficient and unbiased trigger for high energy jets.

The emphasis on jet measurement, which requires a relatively modest energy resolution for electromagnetic showers, led to the choice of a sampling calorimeter for the EMCAL, based on the shashlik principle [31]. The target for the relative energy resolution as a function of energy is $\sigma_E/E = 15\%/\sqrt{E(\text{GeV})} \oplus 2\%$. A significant difference between the ALICE design and the shashlik

implementation of LHCb (Section 4.3.2) results from the fact that the ALICE calorimeter operates in a strong magnetic field, precluding the use of photomultiplier tubes for light detection.

The EMCAL subtends 110° in azimuth, at a radius of 428 cm from the beam pipe, and extends over the pseudorapidity range ($-0.7 < \eta < +0.7$). It consists of an arch of five full ‘supermodules’ (Fig. 28, centre and right), each covering 20° in azimuth, plus two smaller supermodules, each covering 7° , on either side of the detector centre. A full supermodule comprises 24 ‘strip modules’ each containing 12 modules. Modules are comprised of four independent readout towers, each with a front face of $6 \times 6 \text{ cm}^2$, with $\Delta\eta \times \Delta\varphi = 0.014 \times 0.014$, at $\eta=0$. A module has a fixed width in the φ direction and a taper of 1.5° in the η direction, so that the complete assembly of 12 288 towers is approximately projective to the collision vertex in both η and φ .

The modules are built from 76 layers of lead, 1.44 mm thick, interleaved with 77 layers of scintillator 1.77 mm thick. This arrangement provides a sufficiently fine sampling fraction to reach the required energy resolution and results in a total active detector thickness of 24.6 cm ($20.1X_0$) (Fig. 29). Shower leakage is estimated to lead to a non-linearity in response of $\sim 2.8\%$ for photon energies up to 100 GeV, which is within acceptable limits. The detector has an average active density of 5.7 g cm^{-3} and a Molière radius of 3.2 cm. WLS fibres, 1 mm in diameter, pass longitudinally through the stack and terminate at the front face of the module. The fibres are aluminized (by sputtering at liquid nitrogen temperatures) on their front face to provide a high level of reflectivity, to return the light emitted in the forward direction in the fibres.

At the rear of the module, groups of 36 fibres from each tower are collected and matched to $5 \times 5 \text{ mm}^2$ Hamamatsu S8664-55 avalanche photodiodes which are operated at a gain of ~ 30 . Since analogue tower energy sums form a basis of the ALICE shower trigger, the APD gains are adjusted to achieve a relative uniformity of within 5% for the response of the towers. The APD output is fed to a preamplifier with a shaping time of 200 ns. This is much shorter than the 2 μs peaking time used for the PHOS signals, partly because there are indications that the EMCAL will be affected by a large slow neutron contribution from hadronic showers, having a tail extending for hundreds of nanoseconds after the collision, and partly to reduce the overall data volume.

A measurement of the light collected as a function of depth in a module is shown in Fig. 30 (left). The collection is flat in the important region of the shower maximum, which is 11 cm from the front (at 26 cm on the x -axis), for 10 GeV photons. The light collection rises near the APD end, which may help to compensate for rear leakage of showers at high energies. In a test beam, the average light yield from the central towers in a matrix of 16 production modules (64 towers), was measured to be 4300 photons/GeV. The average resolution, obtained at different impact positions, and summing over 3×3 tower clusters, is shown as a function of energy in Fig. 30 (right). The fitted curve corresponds

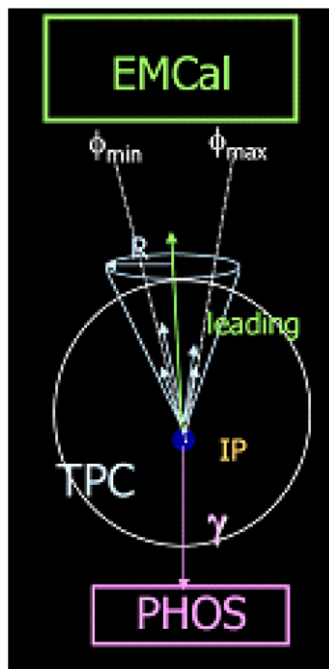


Fig. 27. A drawing illustrating photon-jet physics in ALICE using the Time Projection Chamber (TPC) for charged particle tracking; and the PHOS and EMCAL for photon and jet measurements, respectively.

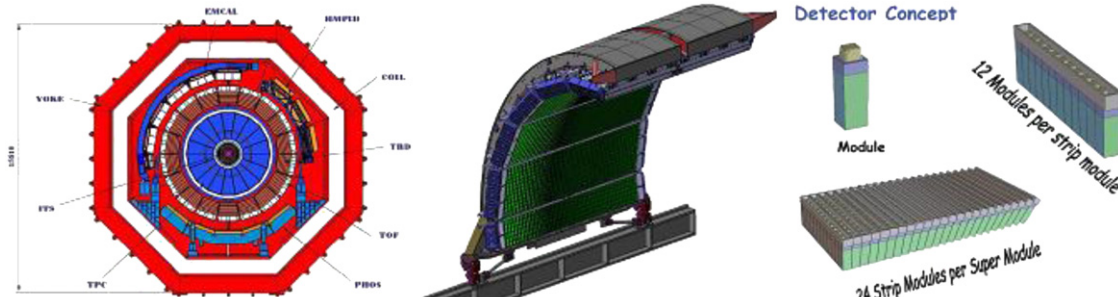


Fig. 28. The location of the EMCAL in ALICE (left); schematic of the EMCAL (centre) and the component elements of a supermodule (right).

to a stochastic term of 11.3% and constant term 1.68%, in line with the target specifications.

4.3.4. The KLOE sampling calorimeter

The KLOE experiment [33] was designed to study CP violation in the decays of neutral kaons, produced through the reaction $\varphi \rightarrow K_L K_S$. It operated at DAΦNE, the $e^+ e^-$ colliding beam accelerator at Frascati, Italy, from 1999 to 2006. The aim was to measure the ratio of direct to indirect CP violation with a precision of 10^{-4} . In order to achieve this goal, it was necessary to keep the systematic uncertainty in the measurement of the branching ratios of $K_{L,S} \rightarrow \pi^+ \pi^-$ and $\pi^0 \pi^0$ below 3×10^{-4} , and the uncertainty for each branching ratio below 10^{-4} . The detector was therefore required to measure very precisely charged and neutral pions with energies up to a few hundred MeV. It comprised two main components, a large 4 m diameter drift chamber and an electromagnetic calorimeter, both inside a solenoid, which provided a magnetic

field of 0.52 T (Fig. 31). The mean decay length of K_L mesons at DAΦNE is 3.4 m and about 30% of K_L mesons decayed within the fiducial volume of the tracker.

The electromagnetic calorimeter [34] is a sampling device, composed of lead foils and scintillating fibres. At first sight, the choice of a sampling calorimeter is surprising, given the requirement for very good energy resolution ($\sim 5\%/\sqrt{E[\text{GeV}]}$) for photons with energies in the range 20–280 MeV. However, the KLOE design has been carefully optimized to give an energy resolution approaching that of homogeneous calorimeters. The calorimeter is also required to have excellent timing resolution ($\sim 50 \text{ ps}/\sqrt{E[\text{GeV}]}$) in order to measure the distance travelled by K_L before decaying to π^0 .

The Barrel calorimeter is a cylinder of 4 m diameter consisting of 24 trapezoidal modules, each 4.3 m long, with a depth of 23 cm ($\sim 15X_0$). The front and rear widths of the modules are 52 and 59 cm, respectively. Each Endcap consists of 32 vertical modules, 23 cm in depth and ranging from 0.7 to 3.9 m in length (Fig. 31).

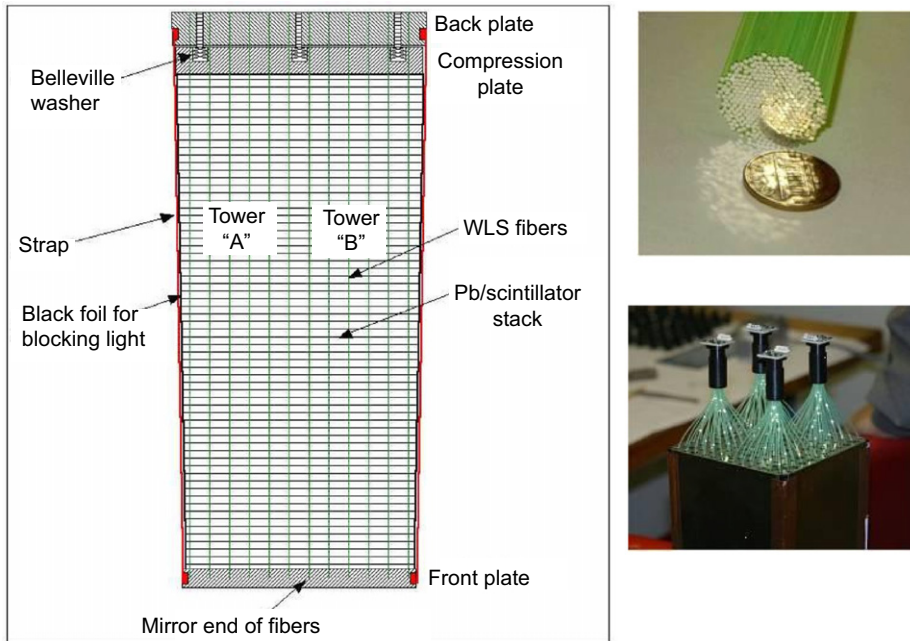


Fig. 29. A diagram of a module stack (left), a set of aluminized WLS fibres (top right) and the connection of the 36 WLS fibres from each tower to the avalanche photodiodes (bottom right).

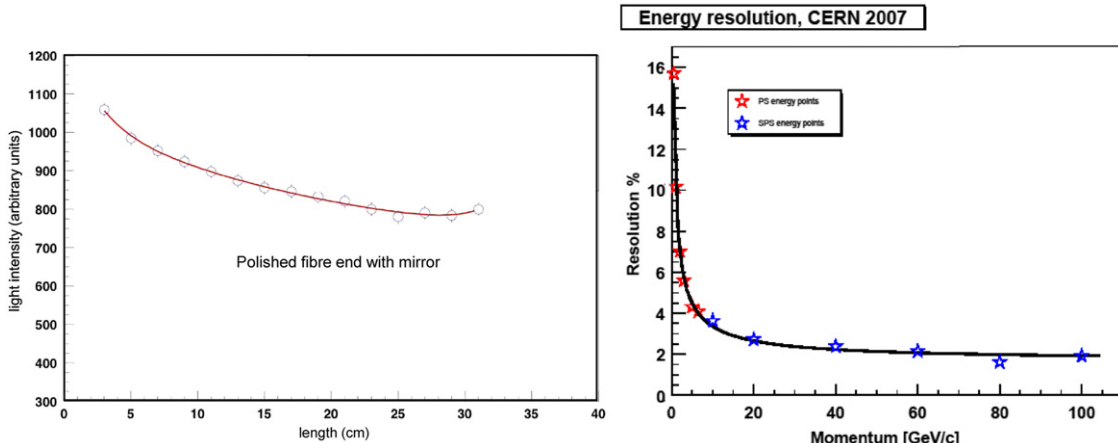


Fig. 30. Left, the light collected as a function of depth in an ALICE EMCAL module, the APD is at 0 cm, the front face of the module is at 37 cm. Right, the average resolution as a function of energy for electrons, measured at a test beam.

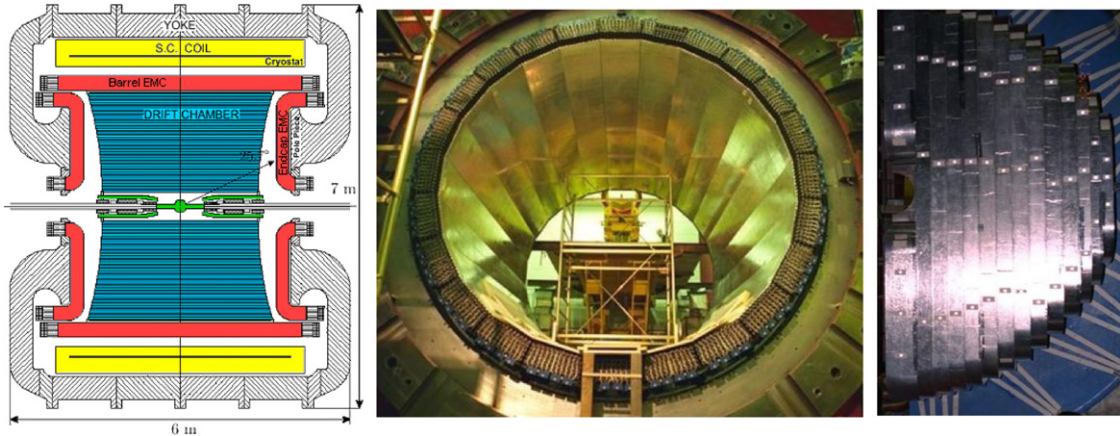


Fig. 31. The KLOE detector, with the electromagnetic calorimeter surrounding the drift chamber (left), a view of the Barrel calorimeter (centre) and part of the Endcap calorimeter (right).

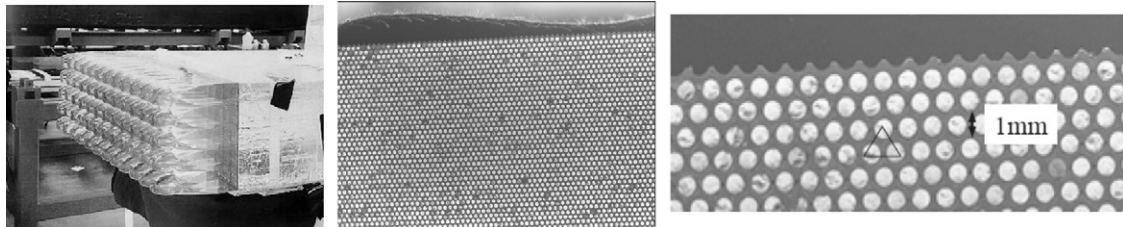


Fig. 32. A photograph of a Barrel module equipped with light guides (left), the end of a machined module before the addition of the light guides (centre), and a close-up of the fine grained matrix of scintillating fibres nestled between corrugated lead sheets. The equilateral triangle has sides of 1.3 mm (right).

The modules consist of stacks of 200 grooved lead foils, 0.5 mm thick, alternating with 200 layers of 1 mm diameter clad scintillator-fibres, which are glued into the grooves (Fig. 32). A total of 15 000 km of fibre and 75 km of 65 cm wide lead foils were used in the construction. Foil thickness was controlled to a few microns and the straightness of the grooves controlled to 0.1 mm per metre of foil length.

The assembly was pliable during the curing time for the glue, allowing the ends of the Endcap modules to be bent (10 layers at a time) by 90°, in order to align the photomultipliers to the direction of the magnetic field and to allow a close fit between the active volumes of the Endcaps and the Barrel. The final dimensions of each module were achieved by milling the sides and end faces and wrapping the long sides with 0.16 mm aluminium foil for light tightness. The full calorimeter covers a solid angle of $\sim 98\%$ of 4π .

In order to have a high scintillator content combined with fine absorber granularity, required for good energy resolution, the lead–fibre–epoxy ratio chosen is 42:48:10. The average density is 5 g cm^{-3} and the radiation length $\sim 1.5 \text{ cm}$. The modules are read out at each end via light guides coupled to fine-mesh Hamamatsu R5946 1.5 in. phototubes. The light yield is ~ 1 photoelectron per mm of traversed fibre for minimum ionizing particles, at a distance of 2 m from the phototube. Light propagation in the fibres is by single mode (which leads to better time resolution), with a velocity of 16.7 cm ns^{-1} . The phototubes are located in cavities in the pole pieces, where the total magnetic field is less than 0.2 T and where the transverse field component is less than 0.07 T. The phototube gains decrease by $\sim 10\%$ when the field is turned on, but linearity and resolution are not affected.

The light guides on the Barrel modules are arranged to provide 5 readout planes, each with 12 light guides, with a similar arrangement on the Endcaps, leading to a total of 4880 readout

channels, or cells, each of $\sim 4.4 \text{ cm}$ width. This segmentation yields a spatial resolution of $\sim 1.3 \text{ cm}$ ($4.4/\sqrt{12}$) for isolated showers, which matches the average lateral shower size in the calorimeter. The measurement of the energy, position and arrival time of a particle is carried out by a clustering algorithm, using groups of contiguous cells and using the longitudinal coordinate obtained from the difference in timing at each end of the module.

The in-situ energy resolution for photons, from radiative Bhabha events, is $5.7\%/\sqrt{E[\text{GeV}]}$, with a negligible constant term (Fig. 33, left). The resolution is mainly associated with sampling fluctuations, receiving a lesser contribution from the photoelectron statistics ($\sim 2000 \text{ p.e./GeV}$). The timing resolution obtained with photons from radiative φ decays is $54 \text{ ps}/\sqrt{(E[\text{GeV}]+140 \text{ ps})}$ (Fig. 33, right). The contribution of the constant term to the timing resolution arises mainly from the length of the collision region in DAΦNE. The intrinsic time resolution is calculated to be $54 \text{ ps}/\sqrt{E[\text{GeV}]+50 \text{ ps}}$, giving a position resolution for electromagnetic showers of $\sim 9 \text{ mm}/\sqrt{E[\text{GeV}]+8.4 \text{ mm}}$ along the longitudinal direction of the modules. The absolute energy scale of the calorimeter is determined from 2γ events, using the precisely known φ mass ($1019.417 \pm 0.014 \text{ MeV}$) as reference. The more abundant Bhabha events (which suffer more energy loss in upstream material) are used to determine relative cell responses.

An illustration of the calorimeter performance is given in Fig. 34 (left), which shows the di-photon mass reconstructed in $\eta \rightarrow \gamma\gamma$ decays produced from $\varphi \rightarrow \eta\gamma$, by performing a kinematic fit using the positions, times, and energies of the three photons. The small width results mainly from the precision of the position measurements. The value obtained for the η mass is $547.853 \pm 0.024 \text{ MeV}$ [35].

An example of the topological reconstruction of K_L decays, from $\varphi \rightarrow K_L K_S$, is illustrated in Fig. 34 (centre and right). The direction of the K_S is measured from its decay to two

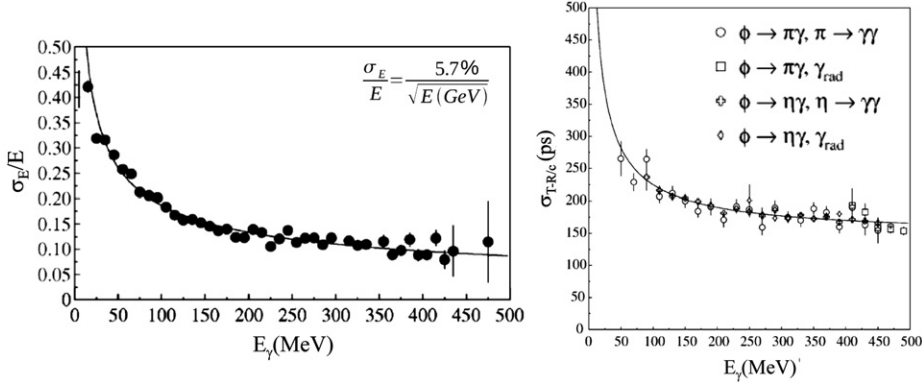


Fig. 33. The energy resolution and timing resolution for the KLEO calorimeter using the photons from radiative ϕ decays.

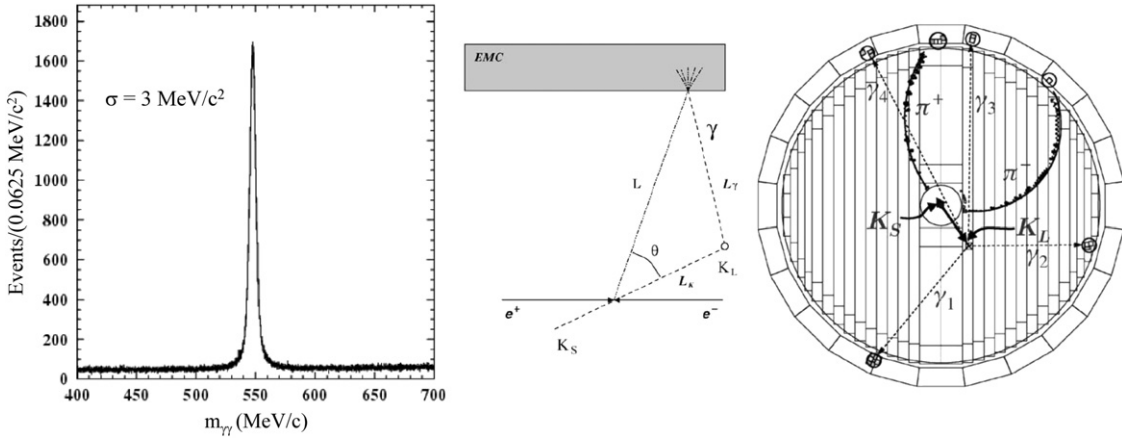


Fig. 34. The reconstructed η mass peak (left), the constraints for $\phi \rightarrow K_L K_S$ reconstruction (centre) and a fully reconstructed $\phi \rightarrow K_S K_L$ event to two electrons and four photons (right).

electrons. The K_L moves in the opposite direction. The position of its decay is then determined from the relative timing of the four photons from $K \rightarrow \pi^0 \pi^0$ measured in the calorimeter. The fully reconstructed event is shown in Fig. 34 (right).

4.4. Particle flow calorimetry at the International Linear Collider

4.4.1. Introduction

The International Linear Collider (ILC) is a proposed machine, based on superconducting accelerating cavities, that will provide e^+e^- collisions at beam energies up to 500 GeV [36]. A Global Design Effort (GDE) is currently underway, with the objective of publishing a Technical Design Report at the end of 2012. Within this framework, the International Detector Advisory Group (IDAG) considered Letters of Intent for ILC detectors. In August 2009, IDAG validated two designs: the International Large Detector (ILD) [37] and the Silicon Detector (SiD) [38], and invited the two collaborations to proceed towards a baseline design by 2012.

The purpose of the ILC is to extend and complement the physics reach of the LHC in areas such as electroweak symmetry breaking, supersymmetry and searches for extra dimensions, with particular emphasis on precise measurements. Most of the relevant physics processes at the ILC lead to final states involving several jets, thus jet reconstruction and invariant-mass resolution for combinations of two or more jets are primary considerations in optimizing detector design. An explicit detector goal is the capability to separate W and Z hadronic decays. This is to allow measurement of the Higgs production process: $e^+e^- \rightarrow ZH$, in events with four jets, in the presence of background from WW

pairs. The requirement demands a jet energy resolution that is of order 3–4% above 100 GeV [37].

The strategy chosen for achieving the required jet energy resolutions in both the ILD and SiD designs is high granularity Particle Flow Analysis (PFA) [39,40]. In this approach, measurement of the charged particle content of jets is made using the tracking system alone, while the calorimeters are used to measure photons and neutral hadrons. The vital ingredients in the PFA approach are the correct matching of charged particle calorimeter clusters to tracks, and the efficient separation of nearby clusters produced by charged and neutral particles. As a consequence, greater weight is given in the optimization of the calorimeter design to having fine granularity than to achieving the best possible single particle energy resolution. Here we concentrate on the implications for the electromagnetic calorimeters, where the PFA strategy results in designs that are significantly different from those adopted by the LHC experiments.

For both ILD and SiD, the priority given to granularity compared to single particle energy resolution has led to the choice of a sampling electromagnetic calorimeter with absorber plates of tungsten. Not only does tungsten have a very short radiation length ($X_0=3.5$ mm), minimizing the depth required, but it has the smallest Molière radius ($R_M=9$ mm) of any practically available and affordable material, enhancing the separation of electron and hadron energy deposits. The two detector groups are currently considering more than one choice of technology for the ECAL active layers. Both ILD and SiD are considering two types of silicon sensor, namely high resistivity silicon pad diodes, and CMOS active pixel devices. In addition, ILD is exploring the use of scintillator strips with novel Geiger-mode photodiode readout.

4.4.2. The ILD electromagnetic calorimeter

An example of an algorithm developed to study PFA at the ILC is PandoraPFA, which has recently been applied to the ILD conceptual design [39]. The performance of several variations of the basic configuration has been studied in detail. A representative schematic drawing is shown in Fig. 35. At the heart of the design is a superconducting solenoid, with a coil having an internal radius of approximately 3.5 m, providing a magnetic field of 3.5 T. An important feature of the layout, which follows from applying PFA criteria to optimize the design, is the location of both the ECAL and the HCAL within the magnetic field volume, immediately adjacent to the tracking system.

The cost and complexity of the calorimeters rise as the number of channels is increased, thus the transverse segmentation should not be finer than that required to keep the contribution to the resolution function from the “confusion” term below an acceptable limit. (The confusion term arises from the masking of

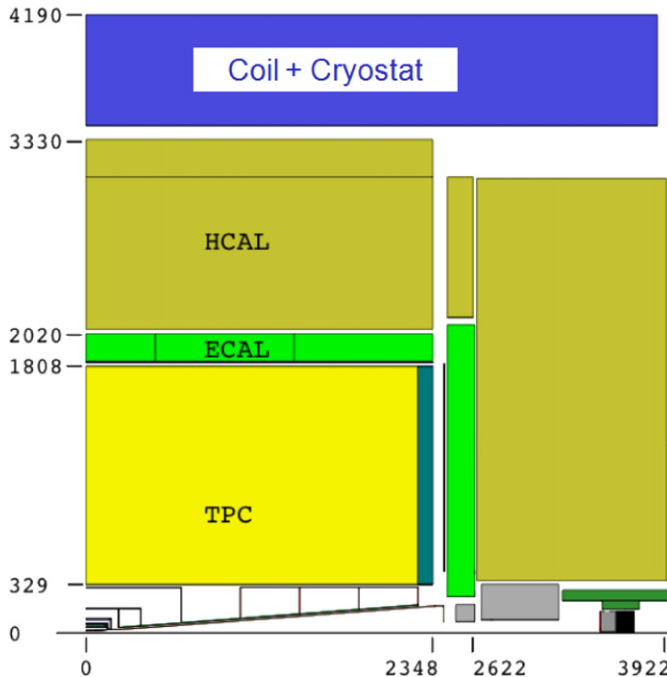


Fig. 35. Conceptual design layout of a quadrant of the ILD detector showing the disposition of the tracking system, calorimeters and superconducting coil. Indicative dimensions are in mm.

photon and neutral hadron calorimeter clusters by charged hadron clusters and from the misclassification of charged hadron clusters as neutral hadron clusters.) It is found that the jet energy resolution continues to improve with decreasing ECAL cell size down to $5 \times 5 \text{ mm}^2$ (Fig. 36, left). In the case of the HCAL, a cell size of $30 \times 30 \text{ mm}^2$ would be adequate for a design option using analogue readout of scintillator tiles (Fig. 36, right). However, alternative designs, based digital readout of gaseous devices, require smaller cell sizes of order $10 \times 10 \text{ mm}^2$.

With these cell sizes, jet reconstruction studies have been performed at four energies (45, 100, 180 and 250 GeV). The results can be described by a semi-empirical parameterization of the jet energy resolution of the form:

$$\delta_{90}E = \frac{21\%}{E} \oplus 0.7\% \oplus (0.004E)\% \oplus 2.1\left(\frac{E}{100}\right)^{0.3}\% \quad (26)$$

where E is in GeV, and the four terms correspond to the intrinsic calorimetric resolution, imperfect tracking, hadron energy leakage and confusion, respectively. ($\delta_{90}E$ is defined as the rms of the reconstructed energy distribution in the smallest range that contains 90% of the events, and is chosen to avoid overemphasis of non-Gaussian tails.)

The function of Eq. (26) is shown by the solid line in Fig. 37 (left), where it can be seen that the goal of better than 3.8% for the jet energy resolution is achieved for energies in the range 40–400 GeV. At a jet energy of 100 GeV the resolution is almost a factor of two better than the resolution that would be obtained using the calorimeter information alone (indicated by the dot-dashed line), demonstrating the power of the PFA approach. The invariant mass distributions for vector bosons reconstructed from pairs of quark jets in simulated $ZZ \rightarrow d\bar{d}v\bar{v}$ and $WW \rightarrow u\bar{u}v\bar{v}$ events are shown in Fig. 37 (right) for boson energies of 125 GeV, typical of the energy of bosons of interest produced in e^+e^- collisions at 500 GeV. The mass resolution (δ_{90}) of 2.8 GeV is compatible with that expected from the jet energy resolution, taking into account the intrinsic width of the bosons, and confirms that the objective of W/Z separation in hadronic decays is achievable.

4.4.3. CALICE studies of a prototype fine-grained ECAL

The development of particle flow algorithms has relied heavily on Monte Carlo simulations of particle shower development and detector performance. It is therefore important to crosscheck the modelling details with appropriate measurements made with practical fine grain calorimeter designs. The CALICE (CAlorimeter for LLinear Collider Experiment) Collaboration has therefore been conducting an extensive test beam programme to study the response

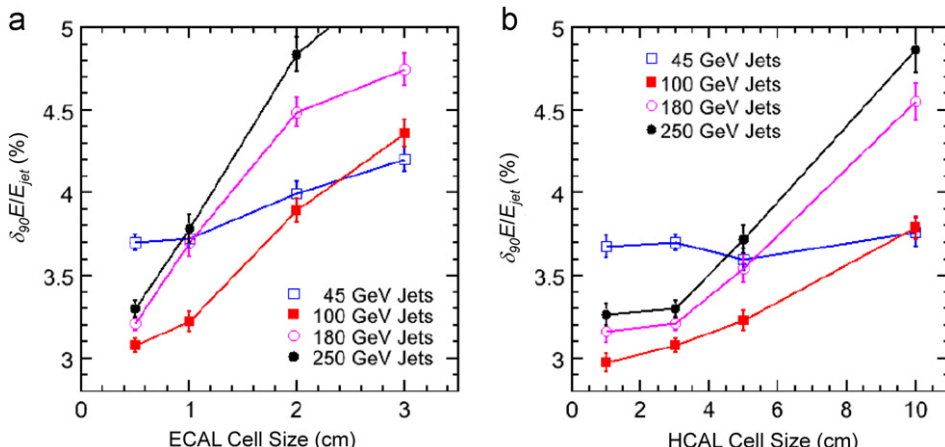


Fig. 36. The dependence of the energy resolution on the calorimeter transverse segmentation for jets from $Z \rightarrow u\bar{u}, d\bar{d}, s\bar{s}$ decays obtained from a simulation of ILD using PandoraPFA [39]. Left: ECAL (silicon pad size), right: HCAL (scintillator tile size).

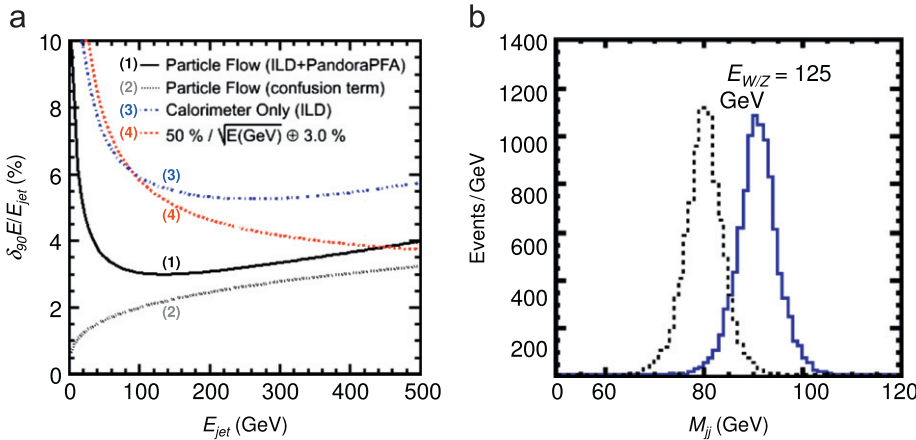


Fig. 37. Simulations of the performance of the ILD calorimeters from Ref. [39]. Left: jet energy resolution versus energy. The solid line is a parameterization of the PandoraPFA result (Eq. (26)). The dotted line (2) is the PFA contribution from the confusion term. The dot-dashed line (3) is the resolution obtained using calorimeter information alone. The dashed line (4) typifies the result expected with a conventional analysis. Right: di-jet mass distributions for W and Z bosons with an energy of 125 GeV, from $ZZ \rightarrow d\bar{d}, v\bar{v}$, and $WW \rightarrow d\bar{d}, v\bar{\mu}$ simulated events.

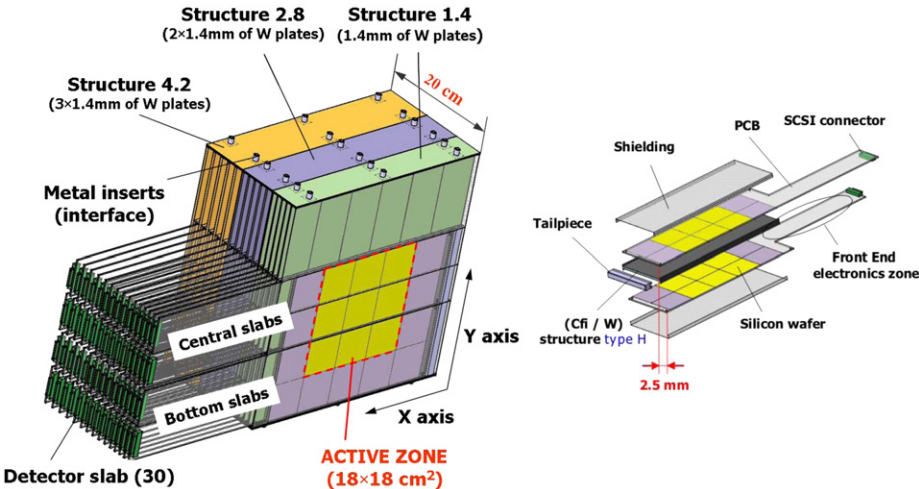


Fig. 38. The CALICE silicon/tungsten ECAL prototype. Left: Schematic view. Only the set of central slabs was mounted for the 2006 beam tests. Right: Detailed view of a "slab", consisting of two printed circuit boards carrying silicon wafers, mounted on either side of a tungsten plate.

of complete calorimeter systems to electrons, muons and hadrons. The goals are to establish the technology for constructing finely segmented calorimeters, and to benchmark and improve particle cascade models and PFA algorithms.

As part of this programme, tests were made on a silicon/tungsten sampling electromagnetic calorimeter in beams at CERN, DESY and Fermilab during the period 2005–2007 [41,42]. This prototype [43] contained 30 layers of tungsten, graded in thickness from front to back ($10 \times 1.4 \text{ mm}$, $10 \times 2.8 \text{ mm}$, $10 \times 4.2 \text{ mm}$), giving a total depth of $30X_0$. The active layers consisted of 30 planes of PIN diode pads, $525 \mu\text{m}$ thick, interleaved with the tungsten plates. The sensors were in the form of 4 in. wafers, segmented into 6×6 pads, each with an area of $1 \times 1 \text{ cm}^2$. There were 3×2 wafers in each layer, providing 18 pads horizontally and 12 pads vertically, giving a total of 6480 pads. The arrangement is shown schematically in Fig. 38 (left).

The silicon wafers were carried on printed circuit boards, 2.1 mm thick. The unit of construction was a "slab" consisting of a silicon plane mounted on either side of a tungsten plane (Fig. 38, right). The slabs were then inserted into spaces between the remaining 50% of the tungsten planes, which were incorporated into carbon-composite support structures, resulting in an

overall calorimeter depth of 20 cm. The two silicon planes in a slab were offset by 2.5 mm in the x direction to avoid alignment of the $\sim 2 \text{ mm}$ gaps between wafers.

The CERN studies were performed with electrons at eight beam energies in the range $6\text{--}45 \text{ GeV}$. The energy deposited in the calorimeter was reconstructed by making a weighted sum of the total signal measured in each silicon layer. It was found that, at each beam energy, the distribution of reconstructed energies was well described, in the region of the peak, by a Gaussian curve. The Gaussian fit was made over an asymmetric range $(-\sigma, +2\sigma)$ to reduce sensitivity to pion contamination, radiative losses of electron energy in the beam and possible residual effects of gaps between wafers. Finally, the expected energy spread of the beam was unfolded from the measured width of each energy distribution in order to extract the intrinsic resolution of the calorimeter. The resulting relative energy resolution is shown as a function of beam energy in Fig. 39 (left). It is well described by a parameterization of the form:

$$\frac{\sigma(E)}{E} = \frac{(16.6 \pm 0.1)\%}{\sqrt{E}} \oplus (1.1 \pm 0.1)\% \quad (27)$$

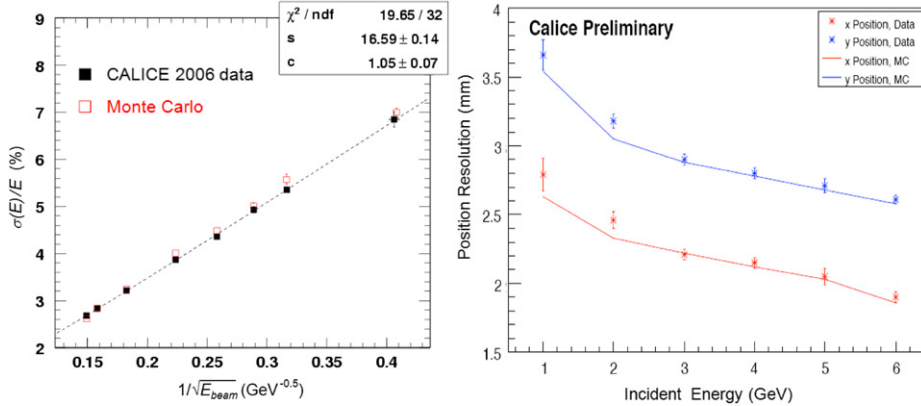


Fig. 39. The performance of the CALICE Si-W ECAL prototype. Left: The relative energy resolution as a function of $1/\sqrt{E}$. The solid black squares are measurements made with an electron beam; the dashed line is a parameterization of these data (Eq. (27)). The open red squares are results from a Monte Carlo simulation. Right: The position resolution as a function of energy. The upper (blue) set of crosses and the lower (red) set of crosses correspond to the vertical (y) and horizontal (x) resolutions respectively. The solid lines are Monte Carlo predictions. (For interpretation of the references to colour in this figure legend, the reader is referred to the web version of this article.)

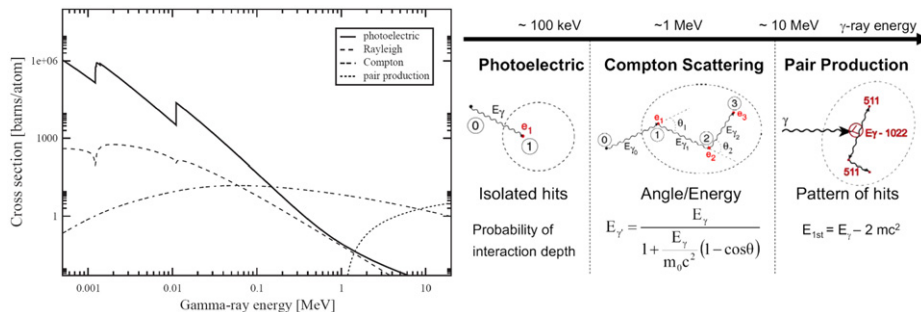


Fig. 40. Interaction cross-sections in Ge for γ -rays up to 20 MeV and, right, illustrations of photoelectric absorption, Compton scattering, and pair production.

The contribution of a possible $1/E$ term was found to be negligible.

Also shown in the figure are the resolutions obtained from a Monte Carlo simulation of the calorimeter performance, based on Geant4. The predicted values agree with the measurements to within 2%.

The primary emphasis of the ECAL prototype design was on implementing the fine transverse segmentation required for optimal PFA performance. Thus, in addition to confirming that adequate energy resolution could be achieved, it was important to study the tracking capability of the calorimeter. To this end, studies were performed at DESY of the spatial and angular resolutions, with normal beam incidence, at 6 energies in the range 1–6 GeV. The shower position and direction at the front face of the calorimeter were reconstructed separately in x and y , event-by-event, from a fit to the shower barycentres measured in each of the sampling layers, and compared to incident tracks measured in four drift chambers upstream of the calorimeter. The ECAL position resolutions, obtained after unfolding the tracking errors, are indicated by the crosses in Fig. 39 (right). The solid lines indicate the predictions of the Monte Carlo simulation and are in excellent agreement with the measurements.

5. Calorimetry for nuclear physics

5.1. Introduction

A widespread application of electromagnetic calorimetry in nuclear physics is in the field of γ -ray spectroscopy. This powerful experimental technique involves the high-resolution measurement

of photons with energies ranging from a few tens of keV to several tens of MeV. In order to achieve the required performance, homogeneous calorimeters based either on scintillating crystals, such as thallium-doped sodium iodide, or semiconductor detectors such as high purity germanium crystals (HPGe) are most commonly used. In general, the approach using HPGe gives the best energy resolution, because, as discussed in Section 3.2, direct detection of the ionization signal results in a small value for the Fano factor.

In the following sections we focus on the AGATA spectrometer, which provides an outstanding example of the application of HPGe detectors to the study of exotic nuclei, to illustrate the latest developments in γ -ray spectroscopy.

5.2. The application of γ -ray spectroscopy to the study of exotic nuclei

Stable atomic nuclei make up most of the visible matter in the Universe. However, their production involves short-lived exotic nuclei, such as those produced by fusion in stars. Understanding the structure of these unstable exotic nuclei may reveal why certain proton-neutron combinations are more stable than others, or have particular shapes, as well as indicating how elements are built up in stars. A common feature of nuclei is that they have a rich complexity of energy levels. Thus de-excitations from a single excited nucleus may result in the cascade emission of 30 γ -rays or more and the superior energy resolution of HPGe detectors makes them an indispensable tool for these studies.

The mean free path in Ge is ~ 25 mm for photons of 1.3 MeV. Thus at this energy, a γ -ray will suffer typically three or four scatters within a 90 mm deep detector (Fig. 40). Above ~ 10 MeV,

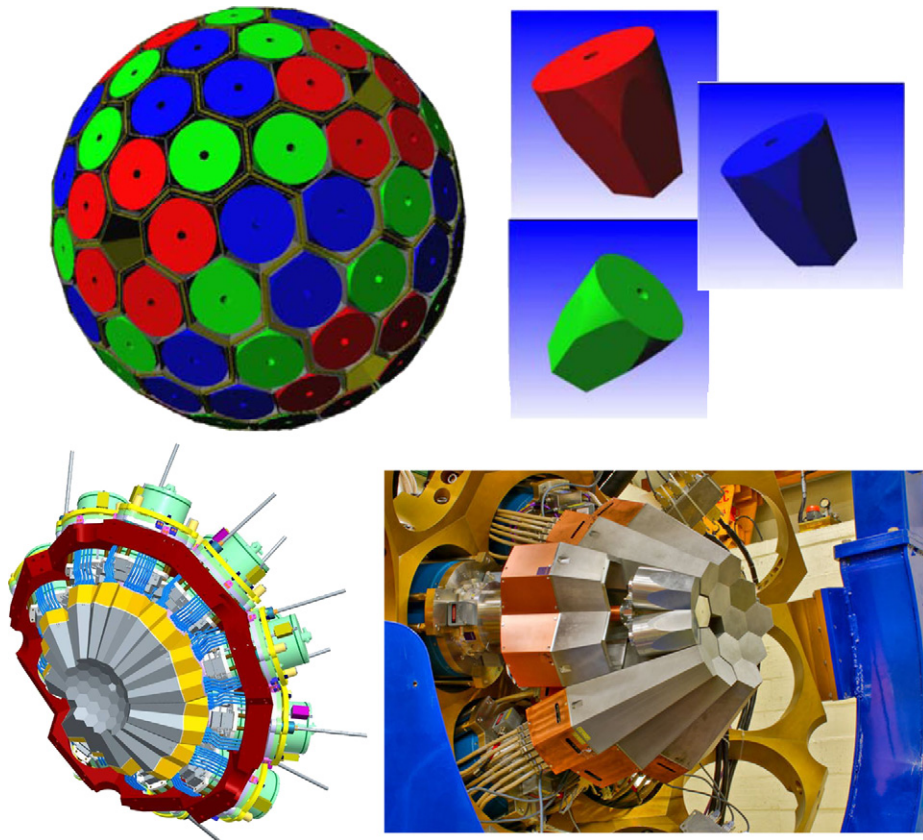


Fig. 41. Top, the arrangement of Ge crystals in AGATA and details of the three shapes that comprise a triple detector; bottom left, the design of an initial 1 π detector, comprising 15 triples; bottom right, a photo showing five mounted triple cryostats (one with its Endcap removed to show the Ge capsules) at Legnaro, Italy.

γ -rays lose energy through pair production, with the resultant electron and positron absorbed within a short distance. Below 10 MeV, γ -rays lose energy through Compton scattering before being totally absorbed through photoelectric absorption at energies below ~ 200 keV.

A major drawback of earlier generations of γ -ray detectors concerned the loss of Compton-scattered photons to regions outside the sensitive volume of the detector resulting in an incomplete energy measurement of the incoming γ -ray. To flag and reject such events the escaping Compton photons were detected by surrounding (and often bulky) veto, or Compton suppression, counters, leading to a substantial loss in detection efficiency.

Modern detector systems being constructed to exploit the new generations of high-intensity radioactive ion beam facilities worldwide, for example at Ganil (SPIRAL) in France, FRIB in the USA, and GSI/FAIR in Germany, will have up to 4 π coverage to minimize the losses due to Compton scatters and fully measure incoming γ -ray energies and directions. The sensitivity of such arrays to detect the weakest signals from exotic nuclear events will be enhanced by factors of up to 1000 relative to previous generations of detectors.

5.2.1. The AGATA tracking calorimeter

AGATA, the Advanced GAMMA Tracking Array [44], is one of the leading examples of the new generation of detectors being assembled for nuclear physics. AGATA is required to have a high efficiency for measuring the full energy of γ -rays over the range of energies expected in the detector. It must have an angular resolution of $\sim 1^\circ$ for measuring γ -ray emission directions in order to correct for Doppler-induced energy shifts. These arise from the recoil of the emitting nucleus, which may have a velocity as large as $\beta \sim 0.5$. The

system must handle high event rates of order 10^6 – 10^7 Hz, in order to detect the weakest reaction channels.

To achieve these requirements, AGATA will cover 80% of 4 π (Fig. 41), with 180 HPGe crystals arranged in 60 tightly packed ‘triples’ on the surface of a sphere of 23.5 cm inner radius. The triples are comprised of three asymmetric shapes to give an optimal geodesic tiling of the spherical surface. The crystals have a total mass of ~ 360 kg. The choice of crystal segmentation, both transversely and in depth, is dictated by the calculated position resolution which depends on the electric field within the crystal and the probability of interaction in each segment (Fig. 42).

5.2.1.1. The HPGe crystal detectors. The characteristics of a single HPGe detector are shown in Fig. 43. The crystal is cut from a cylindrical ingot of n-type Ge, 80 mm in diameter and 90 mm long, to form a 6 sided detector with an 8° taper. The inner contact to the detector is through a 5 mm radius bore hole along the axis of the cylinder which stops at a depth of 13 mm from the front face. The outer surface comprises 36 contacts which segment the crystal laterally into 6 rings with thicknesses from 8 to 18 mm. The 37 channels are read out via fast preamplifiers and sampled with 14-bit, 100 MHz Flash ADCs sited behind the crystals, over a range of ± 1 V (± 10 MeV). The full array of 180 detectors will have a total of 6660 readout channels, with each detector possibly running at up to 50 kHz. A completed triple cryostat comprises the three Ge capsules, the cold FETs and preamplifiers and a liquid nitrogen Dewar to cool the Ge to operating temperature. Construction details of the Ge capsules are shown in Fig. 43.

5.2.1.2. Response uniformity and position resolution. The position of an energy deposit in the detector is determined by pulse shape analysis. The evolution of the signal shape with time is complex

and depends on the electric potential and electric field, which vary throughout the volume of the detector, as indicated in Fig. 44. For a central electrode bias of +5 kV, the electric fields are in the range 1–2 kV/cm throughout most of the crystal volume, although they are substantially higher in the front region. The field strength also depends on the orientation of the field with respect to the lattice direction of the crystal. Electrons drift to the central electrode, and holes drift to the segment electrodes on the periphery, with velocities of $\sim 1\text{--}10 \text{ cm}/\mu\text{s}$.

Maps of response as a function of position were made for a single Ge detector, using 662 keV γ -rays from a ^{137}Cs source with a 1 mm diameter collimator. Data were recorded with the source located successively for 1 min, at a matrix of points forming a 1 mm grid in a plane parallel to the front surface of the detector. Fig. 45 shows maps of single hit density for rings 1, 2, and 3 of the

detector, respectively. A selection was made by requiring the signal collected on the central contact to correspond to energy of at least 650 keV. This cut suppressed events where significant energy was lost from the crystal through Compton scattering, and removed other backgrounds. The plots show the segmentation pattern of the detector and the presence of the core hole for rings 2 and 3. The regions of lower efficiency at the periphery of this single crystal would not be present in a full array.

Maps of crystal response have also been recorded with a collimated ^{137}Cs source in a second set-up. In this arrangement, Compton-scattered photons, depositing an energy of 374 keV in the detector, were selected by tagging the scattered photon of 288 keV in a NaI detector which viewed the crystal through a collimator oriented at 90° to the primary γ -ray direction (Fig. 46). These measurements provide a database for the measured pulse

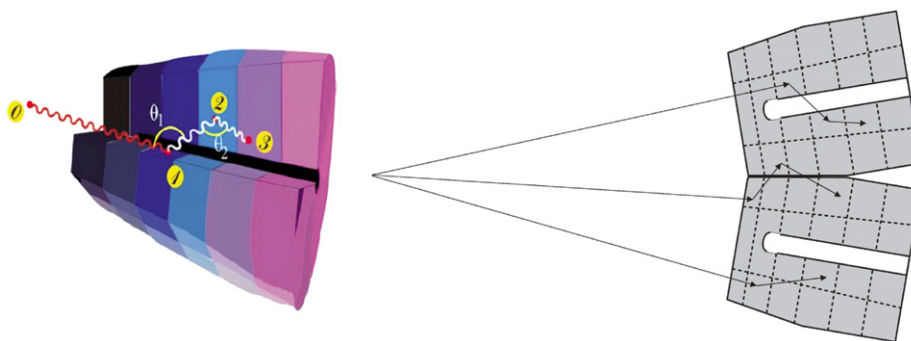


Fig. 42. Left, Compton scattering of an incoming γ -ray in an individual crystal. Right, Compton scattering across crystals for 3 incoming γ -rays.

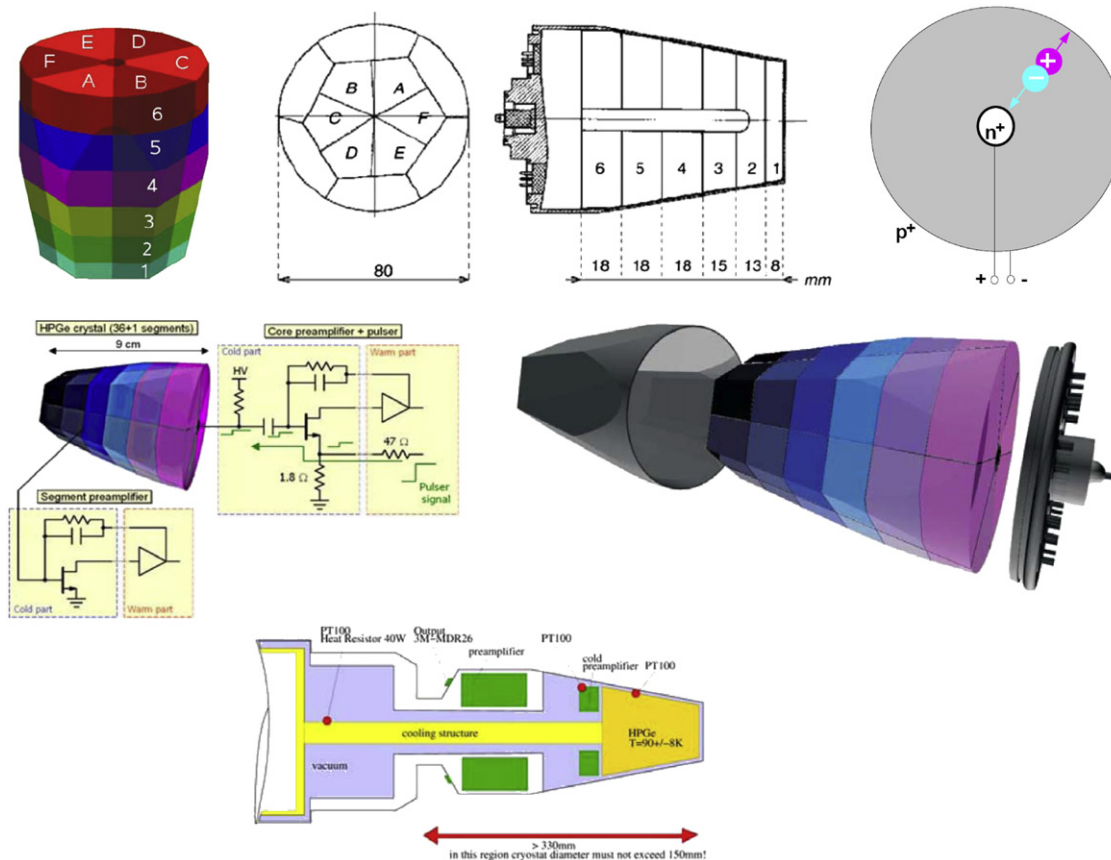


Fig. 43. Construction details of the AGATA HPGe detectors. Top, the segmentation, dimensions, and biasing configuration; middle, the electrical contacts and the encapsulation arrangement, showing an evacuated aluminium canister and feedthroughs; bottom, the arrangement of the readout.

shapes and corresponding positions throughout the active volume of the detector.

In principle it would be possible to calibrate all crystals with this procedure; however, data would be required from $\sim 30\,000$

separate locations. Therefore pulse shapes are calculated instead, using the Shockley–Ramo theorem [45]: the current induced on an electrode by a moving charge at position x and moving with a velocity v , is $qvE_0(x)$, where $E_0(x)$ is the ‘weighting’ field. (The

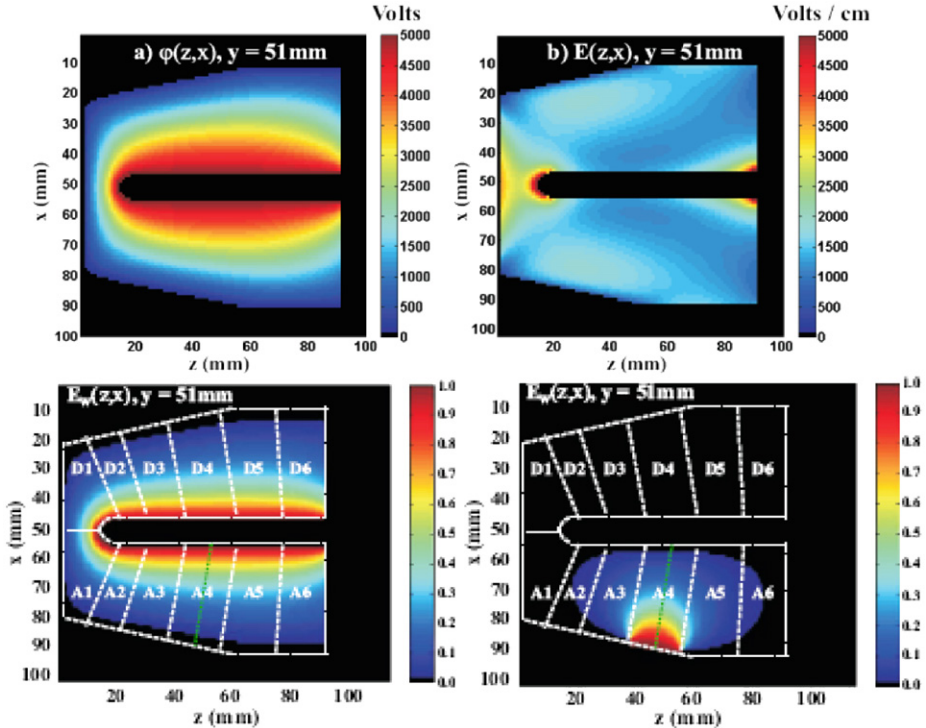


Fig. 44. Top, potential and electric field maps for a central cross-section of a Ge crystal at a bias of +5 kV. Bottom, the calculated ‘weighting’ fields for the anode and for cathode segment A4.

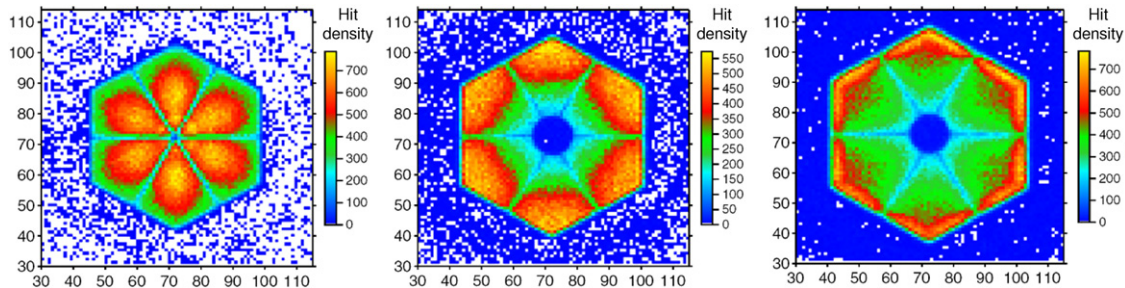


Fig. 45. Single hit distributions for fully contained 662 keV γ -rays in the segments of rings 1, 2 and 3.

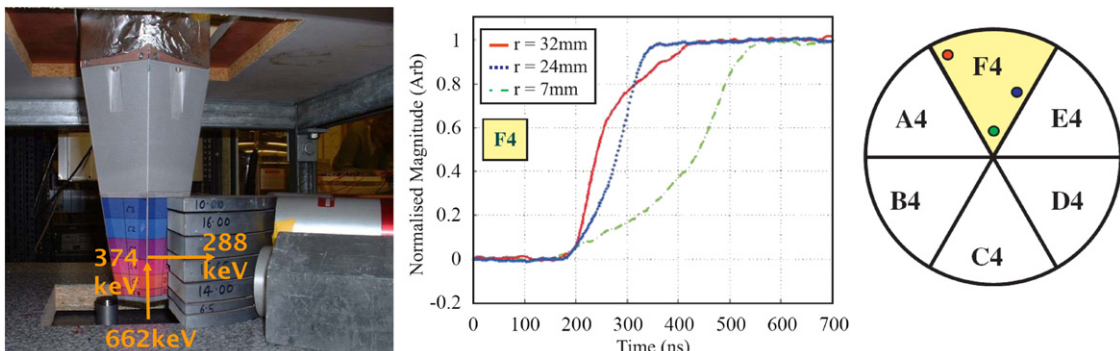


Fig. 46. Left, a test stand for measuring response as a function of position. The incident γ -ray of 662 keV scatters at 90° , leaving an energy deposit of 374 keV in the Ge. Centre and right, the leading edges of pulses measured in segment F4 for three locations within the segment. (For interpretation of the references to colour in this figure, the reader is referred to the web version of this article.)

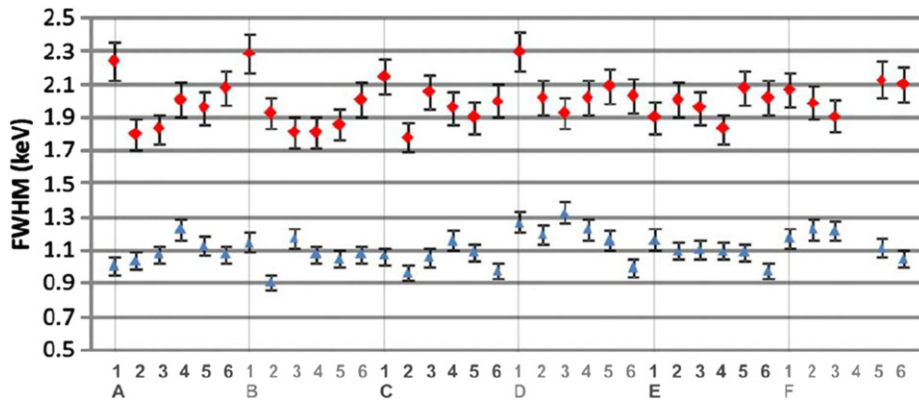


Fig. 47. Energy resolution obtained with γ -rays from ^{241}Am (60 keV) and ^{60}Co (1332 keV), indicated by triangles and diamonds, respectively, for regions in 6 segments of the detector.

weighting is the field that would exist at that position with the selected electrode at unit potential and with all the other electrodes at zero potential and all other charges removed.) Such fields are shown in Fig. 44 (bottom) for the core anode electrode (left) and for cathode A4 (right).

The leading edges of cathode pulses, for three different locations in a segment, are shown in Fig. 46 (centre). The shape of the leading edge for holes drifting from the green circle near the centre of the device to the periphery is markedly different to the shapes for drifts from the red and blue zones nearer the periphery. Comparison is also made with shapes on the core anode and on neighbouring cathode segments for the azimuthal position. The detector position resolution obtained is ~ 5 mm (fwhm) using pulse height analysis. This meets the specification of 1° angular resolution for a nuclear target at a distance of 23.5 cm.

5.2.1.3. Energy resolution. The energy resolution has been measured for each of the segments within a detector, with γ -rays from two sources: ^{241}Am (60 keV) and ^{60}Co (1332 keV) (Fig. 47). The signal distributions have widths of 1.11 and 2.00 keV (fwhm) at energies of 60 and 1332 keV, respectively, corresponding to relative energy resolutions of 0.8% and 0.06% (rms). These results may be compared with expectations based on the discussion of Section 3.2 (Eq. (19)). The energy required to create an electron-hole pair in Ge is 2.95 eV, thus a 1332 keV photon liberates 450 000 electron-hole pairs. Assuming a Fano factor of 0.1 for Ge [7], the rms spread is 250 electron-hole pairs, giving an ideal energy resolution of 0.05%, close to the measured value. These data demonstrate that the detector is extremely well optimized.

5.2.1.4. γ -Ray reconstruction. The tracks of charged particles can be reconstructed by measuring the ionization they produce as they traverse the material of a detector. Reconstructing γ -ray trajectories is more difficult, since ionization is only deposited in the region of a few interaction points, separated by distances of up to several centimetres. Furthermore, sophisticated algorithms are required to treat correctly the different types of interaction: Compton scattering (the most likely interaction for the γ -rays of interest), pair production and photoelectric absorption.

In AGATA, pulse shape analysis is used to reconstruct the energy, timing and spatial information for each interaction. Hits are associated with γ -rays using the Compton scattering formula (Fig. 40 (right)), and the final interaction through photoelectric absorption is also included. The electrons liberated at each Compton scatter have a range of ~ 1 mm and appear as localized energy deposits.

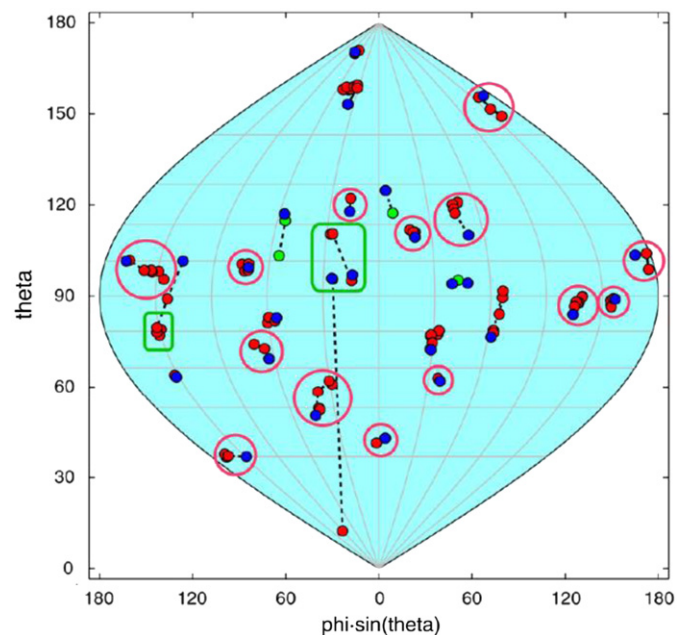


Fig. 48. 'World map' view of the simulated reconstruction of 30 γ -rays of 1 MeV from a nuclear de-excitation in a complete 4π AGATA array.

For γ -ray energies below 150 keV, the photoelectric effect dominates. The resulting isolated single hits are difficult to identify and are assigned using the interaction probability for that energy and location in the detector. Pair production is more important than Compton scattering above ~ 9 MeV. In practice pair production only needs to be considered at the first interaction since its cross-section falls rapidly with energy. It has a unique signature associated with the emission of two collinear 511 keV photons, resulting from the subsequent annihilation of the positron.

Results from the reconstruction in a complete 4π AGATA detector of a simulated event with 30 γ -rays of 1 MeV are shown in Fig. 48. Correctly reconstructed nuclear transitions corresponding to clusters containing the full energy of the γ -ray are indicated by circles on the 'world map', and partially reconstructed γ -rays by rectangles.

5.2.1.5. AGATA performance. The Doppler corrections discussed in Section 5.2.1 are crucial to the achievement of the full performance potential of the AGATA array. Calculating these corrections

requires knowledge of the angle of γ -ray emission with respect to the velocity of the excited nucleus (determined by beamline detectors or inferred from measurements of known nuclear transition lines). An example of Doppler correction is shown in Fig. 49 for γ -rays emitted from ^{49}Ti nuclei with $\beta=0.06\text{--}0.07$ [46]. Using pulse shape analysis to establish the precise location of the first interaction point, the measured width of the 1382 keV line is 4.8 keV (fwhm). This may be compared with the values of 14 or 35 keV that would be obtained if the γ -ray direction were determined using only struck segment or struck crystal information, respectively.

The five-triple prototype AGATA array has undergone tests using the stable beams at Legnaro. The performance of the spectrometer has fulfilled its design aims and AGATA has now

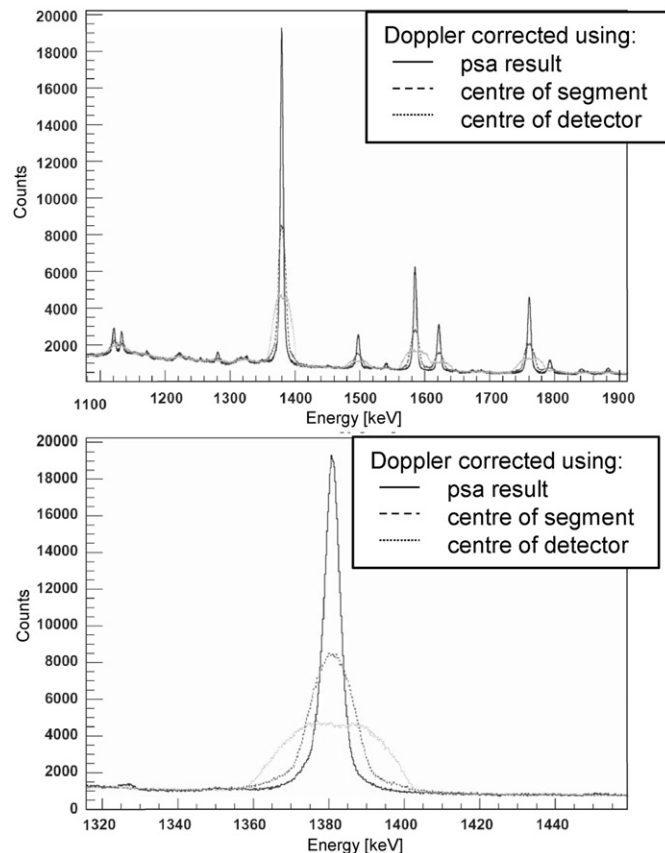


Fig. 49. Top, Doppler corrected spectra for clusters assuming the γ -ray impact point to be at the centre of the Ge detector (dots), the centre of the struck segment (dashes), and using pulse shape analysis (line); bottom, a detailed view around the peak at 1382 keV.

commenced its first physics operation. In this configuration, the full energy (or photo-peak) efficiency for detecting and correctly assigning all the hits from a single 1 MeV γ -ray will be $\sim 3\%$, including the solid angle coverage of the detector and the efficiency of the detector/clustering algorithms. The efficiency will fall to $\sim 2\%$ for de-excitations involving 30 γ -rays, because of the increased numbers of miss-assigned hits. Of those γ -rays that interact in the detector, over 50% will have fully measured energies.

AGATA will be gradually built up towards the full 4π spectrometer and will be used at several laboratories in Europe in a series of experimental campaigns. The first campaign is at Legnaro and the current plans are to move to the GSI Laboratory in Germany in late 2011 and subsequently to the Ganil laboratory in France in 2013.

5.3. Future applications of germanium detector technology

Germanium technology is being considered for the next generation of experiments dedicated to the search for neutrinoless double beta decay. Such decays would produce single energy deposits in a Ge detector. An important potential background arises from photons from radioactive decays undergoing Compton scattering in the detector and leaving multiple energy deposits. The use of pulse shape analysis would help to recognize such events and reject them.

The Majorana collaboration [47] intends to build an array of 57 Ge crystals (60 kg) as a precursor to an experiment with an active mass of one ton or larger. The GERDA (GERmanium Detector Array) collaboration [48] is about to start testing Ge detectors in a cryostat with the eventual goal of building an array of 200 closely packed Ge detectors with a total mass of 500 kg.

6. Calorimetry for low energy neutrino physics

6.1. Liquid scintillator calorimeters

Calorimetry plays a crucial role in neutrino physics. This is exemplified by organic liquid scintillator calorimeters where the liquid provides both the neutrino target mass and the detection medium. In these homogeneous detectors, neutrino events can be recorded in the energy range from a few MeV down to ~ 200 keV, a region which is important for the study of solar and reactor neutrinos. This energy range is inaccessible to water Cherenkov detectors such as SuperKamiokande because, for neutrino energies below ~ 6 MeV, the Cherenkov light yield is too small and because the background from intrinsic radioactivity cannot be reduced to an acceptable level. Two state of the art examples of liquid scintillator detectors are Borexino and KamLAND (Fig. 50).

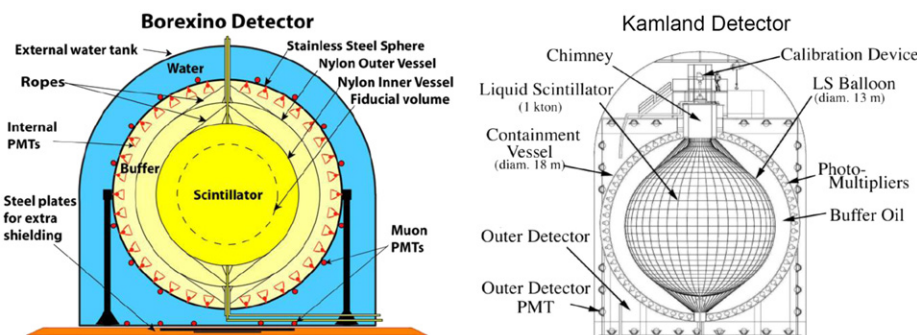


Fig. 50. Borexino and KamLAND neutrino detectors.

6.1.1. The Borexino liquid scintillator detector

The Borexino detector [49] at the Gran Sasso laboratory, Italy, is designed to detect mono-energetic 0.862 MeV neutrinos from the radioactive decays of ^{7}Be in the Sun. These neutrinos account for more than 10% of the solar electron neutrino flux and provide information on the nuclear fusion reactions that power the Sun and on the fundamental properties of neutrinos. The neutrinos are detected through scattering off electrons. The recoiling electron has an energy which depends on the initial energy of the neutrino and varies with the scattering angle. The shape of the electron energy distribution resulting from the scattering of mono-energetic neutrinos is similar to that from Compton scattering of mono-energetic γ -rays.

6.1.1.1. The liquid scintillator. The calorimeter comprises a sphere of 4.25 m radius containing 300 t of ultra-pure organic liquid scintillator held within a thin walled (0.125 mm) Nylon inner vessel (Fig. 50). Surrounding the inner vessel are an outer nylon vessel and a stainless steel vessel, with radii of 5.5 and 6.85 m, respectively, containing two buffer volumes of liquid scintillator. These provide signals that are used to reduce the levels of background from radioactivity in the cavern and to flag and reject events associated with passing muon tracks.

The liquid scintillator is a mixture of solvent (PC – pseudocumene, trimethylbenzene), and fluor (PPO – diphenyloxazole) added at 1.5 g/l (0.17% by weight). The peak wavelength for scintillation emission from this mixture is at 360 nm and the light yield is high (10^4 photons/MeV). It has good transparency, with a mean free path of ~ 8 m for the emitted light, and a fast decay time of ~ 3 ns. These characteristics are essential for good energy resolution, precise spatial reconstruction and for discrimination between events with electrons and background events with alpha particles (Fig. 51).

The liquid scintillator is purified by sparging with high purity nitrogen gas to remove oxygen (which causes scintillator deterioration) and airborne radioactive impurities. The resultant radioactive contamination meets the design goals of $< 10^{-16}$ g/g of ^{238}U and ^{232}Th , and $< 10^{-14}$ g/g of natural potassium – levels that would be very hard to achieve in other calorimetry media. The Nylon for the containment vessel was chosen for its low levels of radioactive impurity and was carefully selected before use.

6.1.1.2. The photo-detectors. The scintillation light is detected by 2212, eight-inch photomultiplier (PMT) tubes (ETL 9351), mounted on the stainless steel vessel (Fig. 52). The photocathode consists of a coating of CsK_{Sb}, deposited on a bulb made of low radioactivity glass (Schott 8246). The peak quantum efficiency of 26% is at 420 nm, well matched to the scintillator emission peak. The PMT radioactive contaminant levels are $< 10^{-9}$ g/g of ^{238}U and ^{232}Th and $< 2.10^{-5}$ g/g of natural potassium.

All but 384 of the PMTs are equipped with conical optical concentrators. These are specially shaped to increase the

collection efficiency of light from the fiducial volume and to reduce the number of photons coming from outside the fiducial volume, such as those originating from radioactive decays in the PMTs. The PMT backgrounds are further reduced by adding a light-suppressant (DMO, dimethylphthalate, 5 g/l) to the outer volume of liquid scintillator, which reduces the scintillation yield by a factor of 20 and reduces the trigger rate due to the intrinsic radioactivity of the PMTs to an acceptable level.

6.1.1.3. Detector performance. An event in Borexino consists of a collection, or cluster, of PMT hits occurring within a time window of a few tens of nanoseconds. Typically ~ 100 hits are recorded within 200 ns for a deposited energy of 200 keV. When there is a trigger, all hits occurring within 16 μs are recorded. The time distribution of hits in a single event is shown in Fig. 53, left. The timing resolution for the rising edge of a cluster is better than 1 ns. Separate clusters as close in time as 15 ns can be identified efficiently. The Borexino main trigger requires at least 30 PMTs to fire, corresponding to an energy threshold of 60 keV and producing a trigger rate of ~ 15 Hz.

The light yield has been determined from a measurement of the decay spectrum of ^{14}C , a naturally occurring and unavoidable background from the hydrocarbon liquid scintillator (Fig. 53, right). The resulting photoelectron yield is ~ 500 per MeV giving a relative energy resolution of $\sim 5\%$ at 1 MeV.

The position of an event in the detector is determined from the arrival times of the scintillation photons at the PMTs. The position resolution has been measured by tagging the radon decay chain of ^{214}Bi and ^{214}Po . The two sequential decays occur in the same place in the detector. Events are selected where Po decays occur within a time interval 5 times longer than the Po lifetime of 235 μs , following the initial Bi decay. Fig. 54 (left) shows the distribution of apparent distances measured between the two co-located decays, giving an average position resolution for the detector of 16 cm.

Signal events are required to be inside a 100 t spherical fiducial region within the 300 t sensitive volume (dotted circle, Fig. 50), and to have only one reconstructed event cluster in order to reject fast coincidence events (for example from the ^{212}Bi – ^{212}Po and ^{85}Kr – ^{85m}Rb decay chains) and accidental pile-up. The resulting spectrum is shown in Fig. 54 (right) after an exposure of 3058 ton-days. The shoulder beyond 560 keV shows the first evidence for the ‘real time’ detection of neutrinos from the radioactive decays of ^{7}Be in the Sun. The observed rate, obtained by combining the results from two analyses, corresponds to $47 \pm 7 \pm 12$ counts per 100 ton-days.

6.1.2. The KamLAND liquid scintillator detector

The Kamioka Liquid scintillator Anti-Neutrino Detector (KamLAND) [50] has been constructed to detect anti-neutrinos generated from nuclear power reactors sited within a radius of 180 km. It is a very large device employing similar techniques to those

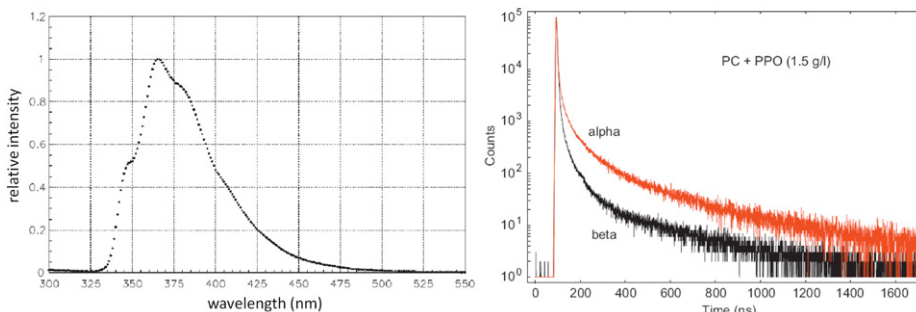


Fig. 51. Left, the emission spectrum for the Borexino liquid scintillator mixture of PC and PPO. Right, the time response for excitation by α and β particles. Pulse shape discrimination techniques, based on the difference in the amount of light emitted at longer times, are used to identify α particles and to reduce backgrounds.

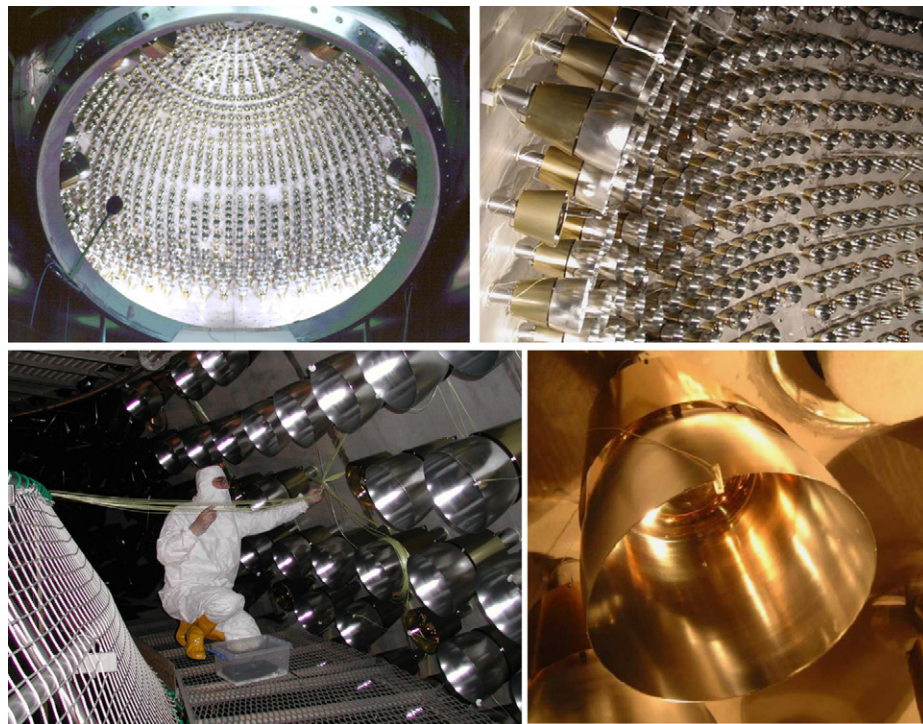


Fig. 52. Top, internal surface of the Borexino stainless steel support sphere showing the PMTs and their optical concentrators. Bottom, preparation of the outer vessel and a close-up of an optical concentrator.

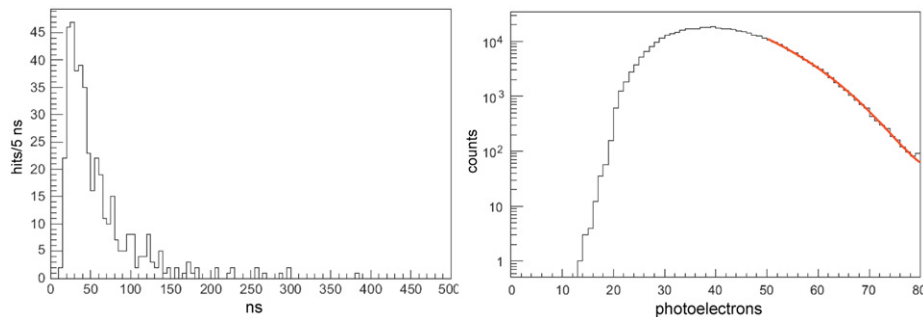


Fig. 53. Left, the time distribution of PMT hits in a single cluster. Right, a fit to the low energy ^{14}C portion of the Borexino spectrum, for events with more than 50 photoelectrons.

used in Borexino, and is located in the Kamioka Mine, Gifu, Japan. The calorimeter comprises 1000 t of ultra-pure liquid scintillator, contained in a 0.135 mm thick Nylon based sphere with a diameter of 13 m, providing a fiducial volume of 408 t.

The scintillation light is detected with 1879 PMTs (Fig. 50, right). The photoelectron yield is $\sim 300/\text{MeV}$, resulting in an energy resolution of $\sim 7.5\%$ at 1 MeV. The energy scale and position resolution is determined by introducing sources at known positions (a technique not accessible to Borexino). The position resolution is ~ 25 cm. The levels of radioactive contamination of the scintillator mixture are $< 3.5 \times 10^{-18} \text{ g/g}$ of ^{238}U and ^{232}Th and $< 10^{-16} \text{ g/g}$ of natural potassium, even lower than those achieved in Borexino.

The hydrogen in the scintillator provides a target of $\sim 3.5 \times 10^{31}$ free protons. Anti-neutrinos are detected through interactions with these protons yielding a prompt positron and a neutron. The neutron is subsequently captured by a proton resulting in the emission of a 2.2 MeV delayed photon within $\sim 210 \mu\text{s}$.

The primary trigger threshold is set at 200 PMT hits, corresponding to an energy of approximately 0.7 MeV. Events are

classified as reactor neutrino candidates if they have fewer than 10 000 photoelectrons (~ 30 MeV), with no signal in the outer detector. A prompt energy threshold of 2.6 MeV is applied to remove neutrino candidates coming from ^{238}U and ^{232}Th decays in the Earth. During an exposure of 162 ton-years, 54 anti-neutrino events were detected, in comparison to 86 expected, setting new constraints on the theoretical models which describe neutrino oscillations.

6.1.3. Liquid scintillator summary

A comparison of the Borexino and KamLAND experiments provides an illustration of the power and versatility of liquid scintillator when used as a combined target and detector in neutrino experiments. In Borexino, it is the electrons in the liquid that serve as the target and the precise timing information is used to reject backgrounds. In KamLAND, the free protons provide the target and the means for detecting the recoil neutrons. In this case, timing information is used to identify the signal and produce the trigger.

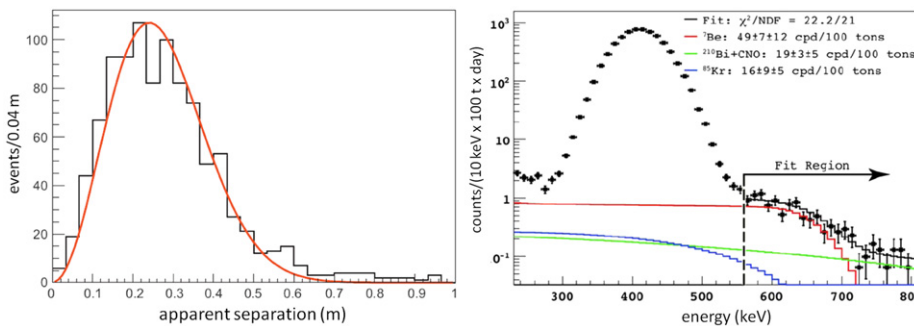


Fig. 54. Left, the distribution of the apparent distances between the two events of the ^{214}Bi - ^{214}Po decay sequence. Right, the spectrum of energies recorded in Borexino after an exposure of 3058 ton-days. The shoulder on the right shows the signal from neutrinos from the radioactive decays of ^{7}Be in the Sun.

7. Summary

In this article, we have reviewed the design and performance of electromagnetic calorimeters from a selection of experiments, chosen to illustrate the state of the art for this class of detector. We have shown that a number of highly developed techniques are available, each with its own particular advantages and limitations. Attention has been drawn to the way in which the physics aims of an experiment influence the choice of technology, and issues have been highlighted that may cause the performance of a practical device to fall short of the ideal values. Overall, the range of energies covered by the different devices is very large. Thus AGATA and Borexino are sensitive to photons with energies as low as 60 keV, MEG is optimized for energies of order a few tens of MeV, and ATLAS and CMS are designed to measure electrons and photons over a range extending from a few GeV to several TeV.

The emphasis has been on applications in particle physics, particularly in experiments at the CERN Large Hadron Collider. However, we trust that workers planning to implement electromagnetic calorimeters in other areas of research will find the material presented here of relevance.

Looking to the future, a promising avenue of development is the Particle Flow Analysis approach, which is already being applied in current experiments such as CMS. The trend towards ever increasing performance of microelectronic components and of computing power will facilitate the design of highly segmented calorimeters and the development of sophisticated reconstruction algorithms needed to realize the full potential of this approach. This is reflected in the strong interest being shown in the technique by the groups developing experiment designs for the ILC.

Acknowledgements

We express our gratitude to the members of the various experiments covered here, who have commented on our distillation of their work and where necessary, corrected our misunderstandings.

References

- [1] B. Rossi, High Energy Particles, Prentice-Hall, 1952.
- [2] Particle Data Group, C. Amsler, et al., Phys. Lett. B667 (1) (2008).
- [3] M.J. Berger et al., XCOM: Photon Cross Sections Database, <http://www.nist.gov/physics/xcom/index.cfm>.
- [4] C.W. Fabjan, in: T. Ferbel (Ed.), Proceedings on Experimental Techniques in High Energy Physics, Plenum, New York, 1985 281, and CERN-EP/85-54.
- [5] W.R. Nelson, et al., Phys. Rev. 149 (1966) 201.
- [6] G. Bathow, et al., Nucl. Phys. B20 (1970) 592.
- [7] H.M. Mann, et al., IEEE Trans. Nucl. Sci. 13 (1966) 252; R.H. Pehl, et al., Nucl. Instr. and Meth. A81 (1970) 329.
- [8] The Compact Muon Solenoid Technical Proposal, CERN/LHCC 94-38, 1994.
- [9] S. Chatrchyan, et al., J. Inst. 3 (2008) S08004.
- [10] A.A. Annenkov, M.V. Korzhik, P. Lecoq, Nucl. Instr. and Meth. A490 (2002) 30; P. Adzic, et al., J. Inst. 5 (2010) P03010.
- [11] Z. Antunovic, et al., Nucl. Instr. and Meth. A537 (2005) 379.
- [12] K.W. Bell et al., IEEE Trans. Nucl. Sci. 51 (2004) 2284.
- [13] The CMS Electromagnetic Calorimeter Technical Design Report, CERN/LHCC 97-33, 1997.
- [14] P. Adzic, et al., J. Inst. 3 (2008) P10007.
- [15] P. Adzic, et al., J. Inst. 2 (2007) P04004.
- [16] ALICE Technical Design Report, <http://aliceinfo.cern.ch/Collaboration/Documents/TDR>.
- [17] D.V. Aleksandrov, et al., Nucl. Instr. and Meth. A550 (2005) 169.
- [18] S. Amerio, et al., Nucl. Instr. and Meth. A527 (2004) 329.
- [19] M. Jeitler, Nucl. Instr. and Meth. A494 (2002) 373.
- [20] B. Hallgren et al., The NA62 liquid krypton calorimeter data acquisition upgrade, in: Proceedings of the Nuclear Science Symposium Conference Record, 2008, NSS'08, IEEE, pp. 2253–2257.
- [21] J. Adam, et al., Nucl. Phys. B834 (2010) 1.
- [22] G. Gallucci, J. Phys. Conf. Ser. 160 (2009) 012011.
- [23] J. Jortner, et al., J. Chem. Phys. 42 (1965) 4250; S. Kubota, et al., Phys. Rev. B 20 (1979) 3486.
- [24] G.J. Alner, et al., Astropart. Part. Phys. 23 (2005) 444.
- [25] G. Aad, et al., J. Inst. 3 (2008) S08003.
- [26] B. Aubert, et al., Nucl. Instr. and Meth. A309 (1991) 438.
- [27] ATLAS Liquid Argon Calorimeter Technical Design Report, CERN/LHCC/96-41, 1996, <http://cdsweb.cern.ch/record/331061>, section 1.10.
- [28] B.C. Allanach, et al., JHEP 09 (2000) 019.
- [29] The LHCb Collaboration, J. Inst. 3 (2008) S08005.
- [30] LHCb Calorimeters Technical Design Report, CERN/LHCC/2000-0036, 2000.
- [31] E. Tarkovsky, et al., Nucl. Instr. and Meth. A379 (1996) 515; A. Bazilevsky, et al., IEEE Trans. Nucl. Sci. 43 (1996) 1491.
- [32] J. Allen et al., Nucl. Instr. and Meth. A615 (2010) 6; The ALICE Electromagnetic Calorimeter Technical Design Report, CERN/LHCC-2008-014, 2008.
- [33] F. Bossi, et al., Riv. Nuovo Cimento 031 (2008) 531.
- [34] M. Adinolfi, et al., Nucl. Instr. and Meth. A482 (2002) 364.
- [35] F. Ambrosino, et al., JHEP 0712 (2007) 073.
- [36] N. Phinney, N. Toge, N. Walker (Eds.), International Linear Collider Reference Design Report – vol. 3: Accelerator, 2007, <http://www.linearcollider.org/cms/?pid=1000437>.
- [37] The ILD Concept Group, The International Large Detector Letter of Intent, DESY2009-87, FERMILAB-PUB-09-682-E, KEK Report 200906, 2010.
- [38] H. Aihara, P. Burrows, M. Oreglia (Eds.), SID Letter of Intent, arXiv:0911.006v1.
- [39] V.L. Morganov, Calorimetry design with energy-flow concept (imaging detector for high-energy physics), in: Proceedings of 10th International Conference on Calorimetry in High Energy Physics (CALOR2002), Pasadena, CA, 2002; J.-C. Briant, Improving the jet reconstruction with the particle flow method: an introduction, in: Proceedings of 11th International Conference on Calorimetry in High-Energy Physics (Calor2004), Perugia, Italy, 2004.
- [40] M.A. Thomson, Nucl. Instr. and Meth. A611 (2009) 25.
- [41] C. Adloff, et al., Nucl. Instr. and Meth. A608 (2009) 372.
- [42] D. Boumediene, J. Phys. Conf. Series 160 (2009) 012065.
- [43] The CALICE Collaboration, J. Inst. 3 (2008) P08001.
- [44] A. Wiens, et al., Nucl. Instr. and Meth. A618 (2010) 223; J. Simpson, J. Nyberg, W. Korten (Eds.), AGATA Technical Design Report Agata/TDR/Dec08/EUJRA, 2008, http://www-w2k.gsi.de/agata/Publications/TDR_EUJRA.pdf.
- [45] Z. He, Nucl. Instr. and Meth. A463 (2001) 250.
- [46] F. Recchia, et al., Nucl. Instr. and Meth. A604 (2009) 555.
- [47] The Majorana collaboration, <http://majorana.pnl.gov/>.
- [48] The GERDA collaboration <http://www.mpi-hd.mpg.de/gerda/>.
- [49] G. Alimonti, et al., Nucl. Instr. and Meth. A600 (2009) 568; C. Arpesella, et al., Phys. Lett. B658 (2008) 101–108.
- [50] K. Eguchi et al., Phys. Rev. Lett. 90, 021802 (2003).